2019

Mode Coupling in Space-division Multiplexed Systems

Huiyuan Liu
University of Central Florida

MODE COUPLING IN SPACE-DIVISION MULTIPLEXED SYSTEMS

by

HUIYUAN LIU
B.S. Tianjin University, 2013

A dissertation submitted in partial fulfillment of the requirements
for the degree of Doctor of Philosophy
in the College of Optics and Photonics
at the University of Central Florida
Orlando, Florida

Fall Term
2019

Major Professor: Guifang Li

ABSTRACT

Even though fiber-optic communication systems have been engineered to nearly approach the Shannon capacity limit, they still cannot meet the exponentially-growing bandwidth demand of the Internet. Space-division multiplexing (SDM) has attracted considerable attention in recent years due to its potential to address this capacity crunch. In SDM, the transmission channels support more than one spatial mode, each of which can provide the same capacity as a single-mode fiber. To make SDM practical, crosstalk among modes must be effectively managed. This dissertation presents three techniques for crosstalk management for SDM. In some cases such as intra-datacenter interconnects, even though mode crosstalk cannot be completely avoided, crosstalk among mode groups can be suppressed in properly-designed few-mode fibers to support mode group-multiplexed transmission. However, in most cases, mode coupling is unavoidable. In free-space optical (FSO) communication, mode coupling due to turbulence manifests as wavefront distortions. Since there is almost no modal dispersion in FSO, we demonstrate the use of few-mode pre-amplified receivers to mitigate the effect of turbulence without using adaptive optics. In fiber-optic communication, multi-mode fibers or long-haul few-mode fibers not only suffer from mode crosstalk but also large modal dispersion, which can only be compensated electronically using multiple-input-multiple-output (MIMO) digital signal processing (DSP). In this case, we take the counterintuitive approach of introducing strong mode coupling to reduce modal group delay and DSP complexity.

To my beloved family.

ACKNOWLEDGMENTS

I would like to express sincere gratitude to my advisor Prof. Guifang Li for being especially motivating, and inspiring throughout my PhD life. He guided me to the interesting research filed of optical fiber communication, and his creative thinking and rigorous academic attitude helped me to finish my Ph.D. study.

I'm also greatly thankful to Dr. He Wen, who taught me a lot in theory and experiment. I feel fortunate to have him in most time of my Ph.D. period, since he is not only a helpful mentor, but also a great friend.

I'd like to thank my committee members, Prof. Patrick L. LiKamWa, Prof. Rodrigo Amezcua Correa, and Prof. Debashis Chanda, for providing helpful suggestions for my final dissertation.

Special thanks go to my colleagues during my time at UCF. Especially senior group members: Dr. Cen (Echo) Xia and Dr. Bin Huang, who helped me understand basics of optical fiber communication and encouraged me to dive deeper. My sincere thanks go to Shengli Fan, Ning Wang, Yuanhang Zhang, Rachel Sampson, Seth Smith-Dryden, and all other previous group members for their valuable discussions, suggestions, and experimental support along the way. Appreciation is due to my collaborators, Dr. Jose Enrique Antonio-Lopez, Juan Carlos Alvarado Zacarias for their significant help with my research work.

Apart from my UCF colleagues and friends, I am also greatly thankful to my advisors during my internships: Dr. Xiang Liu, Dr. Haoshuo Chen, Dr. Nicolas K. Fontaine, and Dr. Roland Ryf, who provided me exciting opportunities to do research and collaborate with brilliant and

enthusiastic researchers. They not only help me gain valuable research experience, but also provide meaningful perspectives towards career and life.

I am forever grateful to my parents, and my sister who loved me, supported me, and respected my decisions. I cannot reach this far and see a larger world without them.

Finally, I would like to thank my wife, and best friend Juan He. I acquired courage and wisdom from her to overcome obstacles in research and life. I am grateful that I have her in the past and the rest of my life.

TABLE OF CONTENTS

LIST OF FIGURES

CHAPTER ONE: INTRODUCTION

Optical fiber communication is the fundamental infrastructure of Internet in contemporary society, meeting daily life and industrial requirements of people around the world. There are more and more bandwidth-demanding applications, like video streaming, online gaming, things of internet, all contributing to the exponentially growing data traffic in the optical fiber. In the past several decades, the capacity in the single-mode fiber (SMF) increases by a factor of 10 every 4 years, which can catch up with fast growing capacity demand of society, as shown in Figure 1.

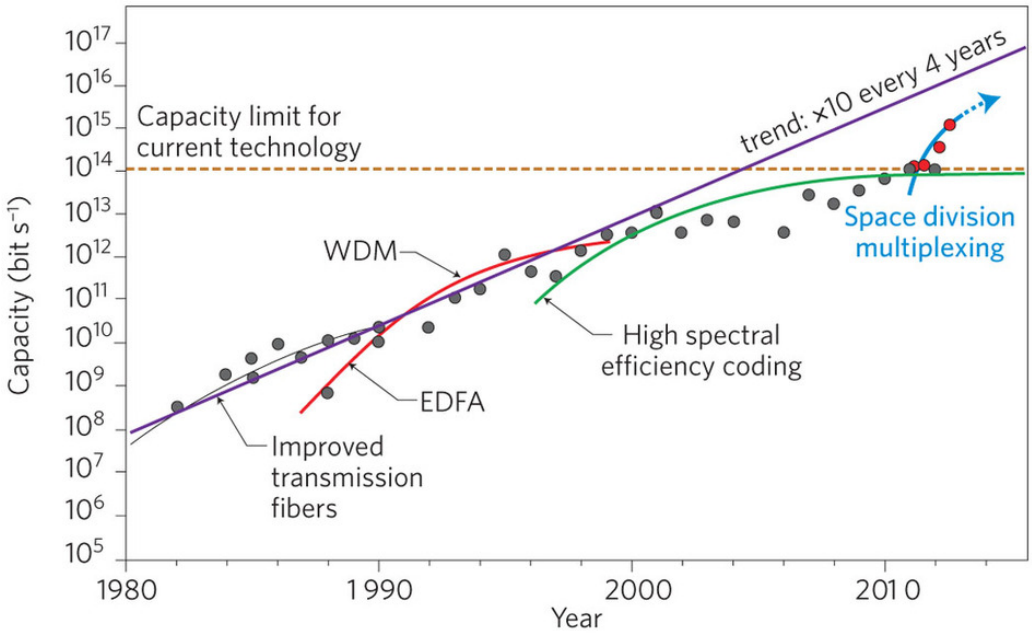

Figure 1: The evolution of transmission capacity in optical fibers with state-of-the-art transmission demonstration [1].

However, nowadays the capacity in SMFs gradually approaches the Shannon's capacity limit, which can be represented by [2, 3]:

$$C = W \log(1 + SNR) \tag{1.1}$$

where W is the bandwidth of the channel, and SNR is the signal-to-noise ratio. From Equation (1.1), to increase capacity, either bandwidth or SNR needs to be increased. For increasing SNR, the direct method is to increase the input power [4]. However, due to the nonlinearity of fiber, the input power cannot be too high. The effective area in SMF can be increased by proper index profile design, or the intrinsic loss of SMF can be reduced by pure silica core [5], to alleviate this problem, bringing larger received SNR. The Erbium-doped fiber amplifier (EDFA) is also an important technique to increase fiber capacity [6, 7], and transmission distance, since it can increase SNR by amplifying optical signal at the transmitter side, receiver side, or along the transmission fiber, making the signal-to-ASE noise the dominating noise rather than the thermal noise [8].

Another method to increase capacity is to enlarge the bandwidth of the fiber. Various degrees of freedom have been exhausted to increase the bandwidth, including wavelength, polarization, quadrature, which are enabled by wavelength-division multiplexing (WDM) [9, 10], polarization-division multiplexing (PDM) and high spectral coding with coherent detection [11], respectively. The combination of difference degrees of freedom can also enlarge the capacity further [12]. The only degree of freedom left is the space, thus space-division multiplexing (SDM) gradually acquires more attention from researchers [1, 13-16], which can use spatial modes in few-mode fibers (FMFs), multi-mode fibers (MMFs), or multi-core fibers (MCFs).

MCFs can be categorized as uncoupled-core or coupled-core MCFs. Uncoupled-core MCFs are similar to SMFs, with a larger core density [17-19], while coupled-core MCFs are similar to FMFs, with supermodes rather than core modes as the mode basis [20-22]. And MMFs can be also regarded as FMFs with a larger number of modes, so the focus is on FMFs here.

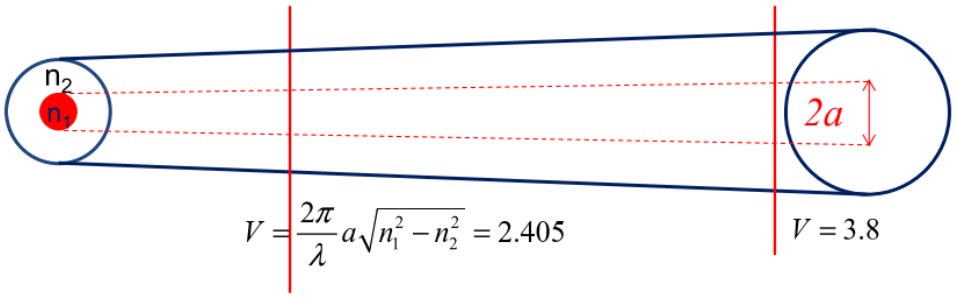

Figure 2: Transition from SMF to FMF by increasing the core diameter [14].

In step-index fibers, the fiber V number can be used to evaluate the quantity of supported modes, defined as

$$V=\frac{2\pi}{\lambda}a\sqrt{n_1^2-n_2^2}, \tag{1.2}$$

where λ is the optical wavelength, a is the core radius, n_1 and n_2 are refractive indices of core and cladding. Nowadays the most widely used fiber in optical communication system is the standard SMF, whose V number is smaller than 2.405, which means that it can only support the fundamental LP_{01} mode in each polarization. As the V number increases due to larger index difference or larger core diameter, the fiber can support more modes, as shown in Figure 2.

Spatial modes are orthogonal to each other ideally in FMFs, which can deliver different signals as independent information channels. However, in realistic FMFs, modes are not perfectly orthogonal, due to unavoidable fiber parameter fluctuation, such as index profile fluctuation, diameter deviation, and microbending, induced by limited fabrication accuracy or random surrounding environment change [23-25]. Those fluctuations would lead to crosstalk between different spatial modes, meaning that the received signal of one mode would also include information from other modes.

Mode crosstalk needs to be effectively managed, to make SDM practical. To address this problem, we need to discuss it in different scenarios. In short-reach systems with a small number of modes such as intra-datacenter interconnects, even though mode crosstalk cannot be completely avoided, crosstalk among mode groups can be suppressed in properly-designed FMFs to support mode group-multiplexed transmission without multiple-input-multiple-output (MIMO) digital signal processing (DSP). Eliminating DSP is very helpful in short-reach systems, since power consumption is a big concern in practical deployment.

However, in most cases, mode coupling is unavoidable. In free-space optical (FSO) communication, mode coupling due to turbulence manifests as wavefront distortions. Since there is almost no modal dispersion in FSO, we demonstrate the use of few-mode pre-amplified receivers to mitigate the effect of turbulence without using adaptive optics.

In fiber-optic communication, MMFs or long-haul FMFs not only suffer from mode crosstalk but also large modal dispersion, which can only be compensated electronically using MIMO DSP after coherent detection. The DSP application-specific integrated circuits (ASICs) have been developed for impairment compensation in SMFs, enlarging the capacity of SMFs in the past [26]. Similar to PDM, SDM can also use DSP ASICs to recover independent information channels, if both amplitude and phase information can be received by coherent detection. Due to large velocity differences of different modes, larger equalizers are required in DSP, which will increase the complexity and cost of the whole system. In this case, we take the counterintuitive approach of introducing strong mode coupling to reduce modal group delay and DSP complexity. So far, there are several methods for reducing the group delay spread (GDS), including optimizing fiber index profiles and modal group delay compensation [27-29]. However, they are only effective

for a small number of modes. The most promising method proposed so far is strong mode coupling. When modes are weakly coupled, the GDS increases linearly with the transmission distance. When modes are strongly coupled, the GDS increases with the square root of the transmission distance, since each mode-division multiplexing (MDM) signal would have a nearly equal probability of traveling on different modes averaged over the transmission link [30].

In this dissertation, the main focus is on tackling the challenges of mode coupling in SDM systems. In chapter 2, FMFs with weak mode coupling is demonstrated, and the relationship between effective area of fundamental mode and effective index difference between first two modes is also studied. In chapter 3, mode-group multiplexing (MGM) transmission in FMFs is demonstrated in short-reach systems. In chapter 4, improving the power efficiency in FSO systems with mode coupling from turbulence, is demonstrated, with the help of few-mode pre-amplified receivers. In chapter 5, strong mode coupling using long-period gratings (LPGs) is demonstrated to reduce modal dispersion in MMFs, to improve the bandwidth of MMFs. In chapter 6, strong mode coupling is also demonstrated to reduce group delay spread in FMFs, to reduce DSP complexity. Chapter 7 summarizes this dissertation.

CHAPTER TWO: FMFS WITH WEAK MODE COUPLING

2.1 Mode coupling in FMFs

The optical fiber can guide light as information carrier due to the total internal reflection at the core-cladding boundary, since the refractive index of core is a little larger than that of the cladding around the core. The number of modes supported in the fiber is determined by the relative index difference between core and cladding, as well as the core diameter. Since the refractive index difference is small, vectorial fiber modes can be simplified by linear polarization (LP) modes under weakly guided approximation.

In an ideal FMF, spatial modes are orthogonal to each other, so there is no crosstalk between different modes, which can be seen from the coupling coefficient calculation [31]:

$$K_{kj} = \frac{w}{4} \iint_{\infty} dxdy \Delta\varepsilon(\mathrm{x},\mathrm{y})\, \vec{\mathrm{e}}_k(\mathrm{x},\mathrm{y})\, \vec{\mathrm{e}}_j^{*}(\mathrm{x},\mathrm{y}), \tag{2.1}$$

where w is the angular frequency, $\vec{\mathrm{e}}_k$ $\vec{\mathrm{e}}_j$ are the transverse components of mode fields labeled k, j, and $\Delta\varepsilon$ is the dielectric perturbation. If there is no or uniform dielectric perturbation, the coupling coefficient is zero. It is the foundation of transmitting different signals in different modes as distinct channels in FMFs. However, those modes are easily coupled to each other in practical FMFs and non-ideal environment, when the dielectric perturbation is not uniform over the cross section of fiber, which affects the system performance of FMFs [32-34]. It may be due to fiber birefringence, core ellipticity, rotation, magnetic field, bending and twisting, which may also induce additional loss [35, 36]. The coupling between modes is also affected by the phase matching condition related to the effective index difference between modes, as shown in coupled-mode equations of two modes:

$$\frac{dA_1}{dz} = iK_{11}A_1 + iK_{12}A_2 \exp\left[i\left(\beta_2 - \beta_1\right)z\right]$$
$$\frac{dA_2}{dz} = iK_{22}A_2 + iK_{21}A_1 \exp\left[i\left(\beta_1 - \beta_2\right)z\right] \tag{2.2}$$

where A_1, A_2 are the amplitudes for two modes, β_1, β_2 are propagation constants of two modes, and coupling efficiencies K_{12}, K_{21} change as $\Delta\varepsilon$. From the coupled-mode equation, the coupling coefficients, which vary along the fiber, need to match the phase terms $\exp\left[\pm i\left(\beta_2 - \beta_1\right)z\right]$ to produce sufficient amplitude change, so the dielectric perturbation or refractive index perturbation that meets the phase match condition brings effective mode crosstalk. Since the dielectric perturbation spectrum as function of longitudinal spatial frequencies has dominant components at low frequencies, increasing the propagation constant difference between modes can reduce the mode crosstalk significantly [37, 38]. To achieve that and ensure same number of modes supported in the fiber, both large index contrast between core and cladding and small core diameter are needed [39].

2.2 Effective area and index difference

In fiber communication systems, large mode effective area benefits the system performance due to the reduced nonlinearity [40]. There were designs for large mode effective area, however [41, 42], they have limitations in SMFs [39], so FMFs attract more attention [43]. For an FMF supporting the same number of modes, increasing effective area needs the reduction of index contrast between the core and the cladding, which would reduce the effective index difference between modes. From previous section, smaller index difference would bring larger

mode crosstalk, so the relationship between effective area and effective index difference needs to be investigated.

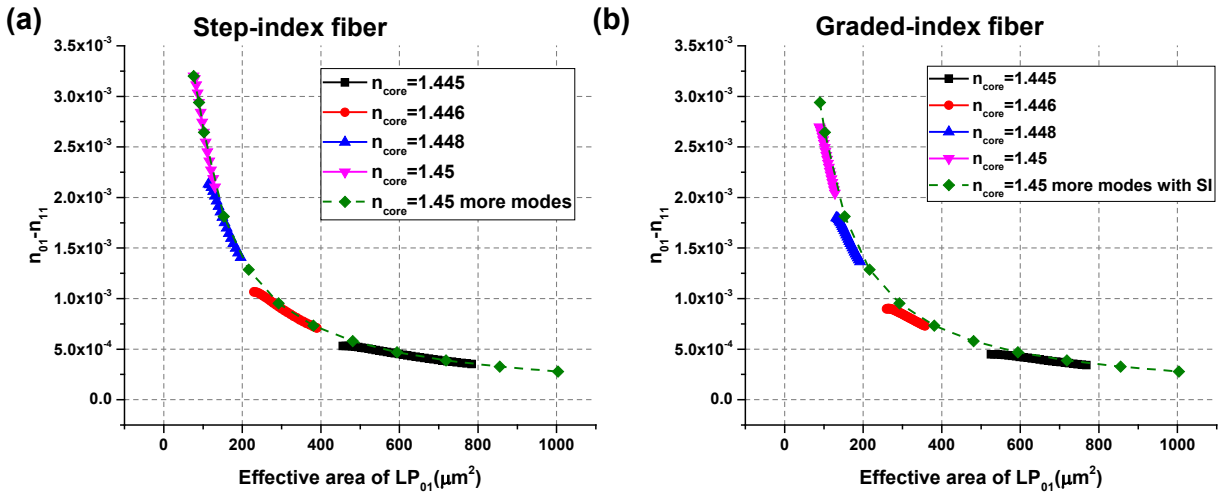

Figure 3: Effective index difference between the first two modes, as a function of the effective area of the fundamental mode, for different core indices with changed core radius for each core index, in (a) two-mode step-index fiber, and (b) two-mode graded-index fiber. Step-index fiber with 1.45 core index and a large range of core radius is plotted as the reference curve.

Usually effective areas of higher-order modes are larger than that of the fundamental mode, since they are less confined by the core [44]. And nonlinearity is more concerned when the optical power is large in long-haul systems, where quasi-single-mode (QSM) transmission plays an important role. So the effective area of the fundamental mode is calculated here. In QSM transmission, the index difference between the fundamental mode and the first higher-order mode is a very important evaluator of the mode crosstalk. For some other applications with graded-index (GRIN) FMFs, there are almost equal effective index differences between neighboring mode groups [45], so the effective index difference between the first two modes is computed here.

Figure 3 shows the effective index difference between first two modes, as a function of the effective area of the fundamental mode in the two-mode step-index (SI) or GRIN fibers. For

different core indices, core radius is changed in a range to ensure only two modes existing. The result of SI fiber with fixed core index of 1.45 and a larger range of core radii is plotted as the reference curve. Other curves are all overlapped with the reference curve, indicating that the multiplication of the effective index difference and effective area is a constant, no matter how the refractive index is varying. Figure 3(b) shows that the constant value for GRIN fiber is very close to and a little smaller than that for SI fiber.

The multiplication of effective index difference and effective area seems to be a constant value for different fiber index profiles, which can be verified analytically. The Helmholtz equation for electrical field E in a GRIN fiber can be written as

$$\nabla^2 \mathrm{E} + n^2 k_0^2 E = \left(\frac{\partial^2}{\partial x^2} + \frac{\partial^2}{\partial y^2} \right) E + (n^2 k_0^2 - \beta^2) E = 0. \tag{2.3}$$

where n is the refractive index represented as $n^2 = n_1^2 - 2n_1^2 \Delta \left(r/a \right)^2$, $\Delta = n_1^2 - n_2^2 / 2n_1^2$, a is the core radius, n_1 / n_2 are refractive indices of core/cladding, k_0 is the wave number, β is the propagation constant. The equation can be also written as [46]

$$-\left(\frac{\partial^2}{\partial x^2} + \frac{\partial^2}{\partial y^2} \right) E + \frac{2k_1^2 \Delta}{a^2} \left(x^2 + y^2 \right) E = (k_1^2 - \beta^2) E. \tag{2.4}$$

where $k_1 = n_1^2 k_0^2$. The solutions can be found as [47]

$$k_1^2 - \beta^2 = 2\sqrt{\frac{2k_1^2 \Delta}{a^2}} \left(m_x + m_y + 1 \right). \tag{2.5}$$

$$\beta = \sqrt{k_1^2 - k_1 \frac{2\sqrt{2\Delta}}{a} \left(m_x + m_y + 1 \right)} \approx k_1 - \frac{\sqrt{2\Delta}}{a} \left(m_x + m_y + 1 \right). \tag{2.6}$$

So the effective index difference between two neighboring modes is

$$\Delta n = \frac{\sqrt{2\Delta}}{ak_0} \tag{2.7}$$

The fundamental solution of the electrical field can be represented as the Gaussian function $E_0 = Ae^{-\frac{x^2+y^2}{2\sigma^2}}$, where σ is the standard deviation of the Gaussian function as $\sigma^2 = \frac{a}{k_1\sqrt{2\Delta}}$ [47, 48].

The integral of a Gaussian function can be written as

$$\iint Ae^{-\frac{x^2+y^2}{2\sigma^2}} \mathrm{d}x\mathrm{d}y = 2\pi A\sigma^2, \tag{2.8}$$

and the effective area of LP_{01} is calculated as

$$A_{eff} = \frac{\left(\iint |E|^2 \, dxdy\right)^2}{\iint |E|^4 \, dxdy} = 2\pi\sigma^2 = 2\pi\frac{a}{k_1\sqrt{2\Delta}}. \tag{2.9}$$

The multiplication of the effective area and index difference thus can be calculated as

$$A_{eff}\Delta n = 2\pi\frac{a}{k_1\sqrt{2\Delta}}\frac{\sqrt{2\Delta}}{ak_0} = \frac{\lambda_0^2}{2\pi n_1}. \tag{2.10}$$

It's a constant with fixed core index and wavelength. When the constant is divided by the wavelength, the formula is only related to core index in the following form

$$A_{eff}\Delta n \Big/ \lambda_0^2 = \frac{1}{2\pi n_1} \tag{2.11}$$

The value would be 0.1098 for 1.45 core index. The fitting curve is plotted in Figure 4(a), showing coefficient fitting result of 0.1097, which is almost same as the analytical result.

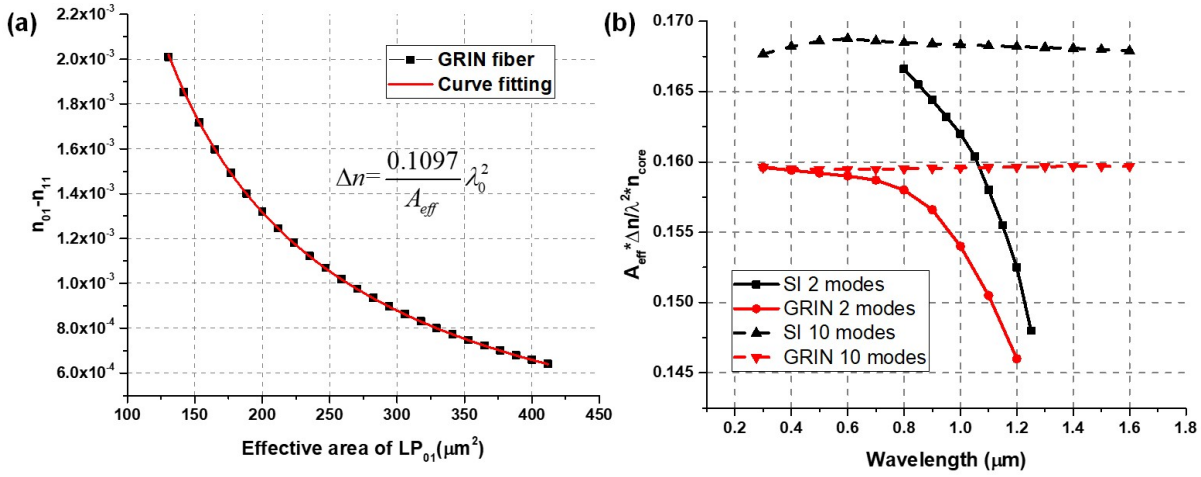

Figure 4: (a) Effective index difference vs. effective area curve fitting for graded-index fiber. (b) The multiplication constant as a function of wavelength for SI or GRIN fibers with 2 or 10 modes.

To verify the formula $\frac{\Delta n A_{eff}}{\lambda_0^2}$ is constant at different wavelengths, the numerical simulation results as functions of wavelength for SI or GRIN fibers with 2 or 10 modes are plotted in Figure 4(b). The curves for 2-mode fibers show that the simulated value decreases slowly as the wavelength increases, because it is closer to the cut-off condition at longer wavelength. Far away from the cut-off condition, the curves of SI or GRIN fibers with 10 modes demonstrate nearly constant values at different wavelengths.

The previous simulation shows that the multiplication of effective index difference and effective area is always a constant for common SI and GRIN FMFs. To generalize the conclusion, various fibers with different index profiles shown in Figure 5(a) are simulated, including two-step fiber, GRIN fiber with a trench outside the core, triangular-size profile, and index profile proportional to the reversed LP_{11} intensity profile. The curves in Figure 5(c) show that the constants for those index profiles are always smaller than that of the SI fiber.

MCFs are also considered, with first supermode profiles for 3-core or 6-core fibers shown in Figure 5(b). The curves of effective index difference vs. effective area are plotted in Figure 5(d). Here the effective index difference is between the first two supermodes, and the effective area is for the first supermode. The results also verify the existence of the limit of the constant no matter what the index profile is.

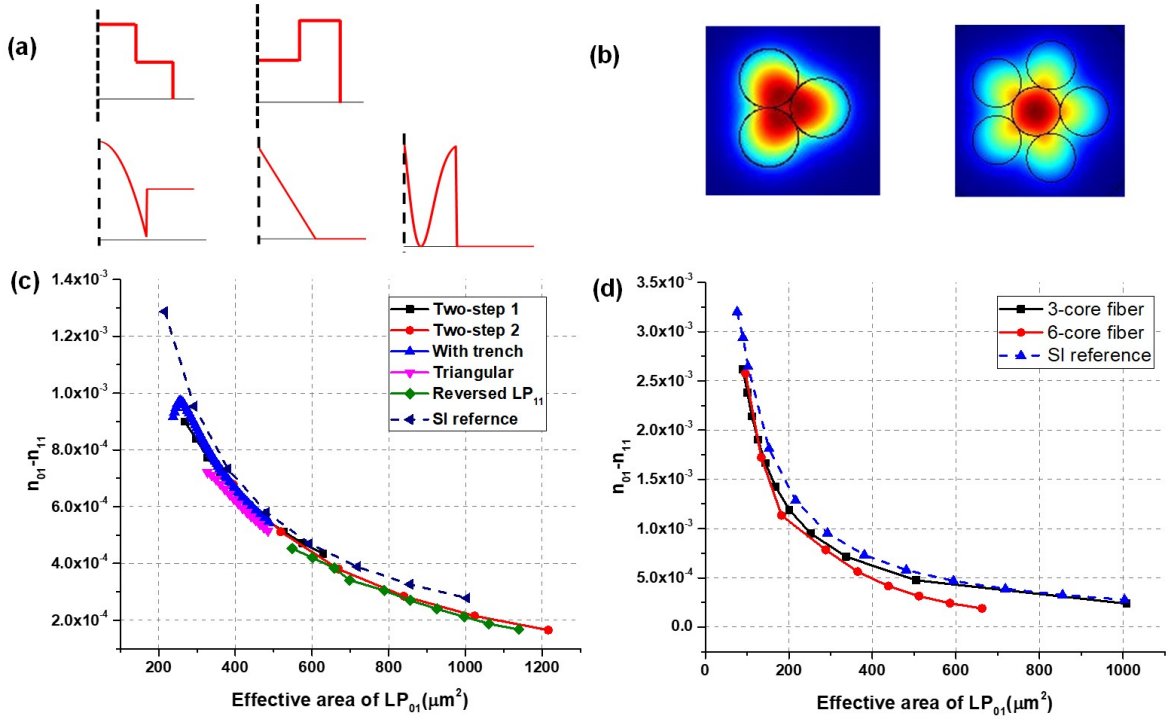

Figure 5: (a) Index profiles for two-step SI fibers (high or low index for the inner step), GRIN fiber with a trench, a triangular-index fiber, and a fiber corresponding to the reversed LP11 mode profile. (b) Mode profiles of the first supermodes in the 3-core or 6-core fibers. Effective index difference vs. effective area for (c) different index profiles in single-core fibers, and (d) MCFs.

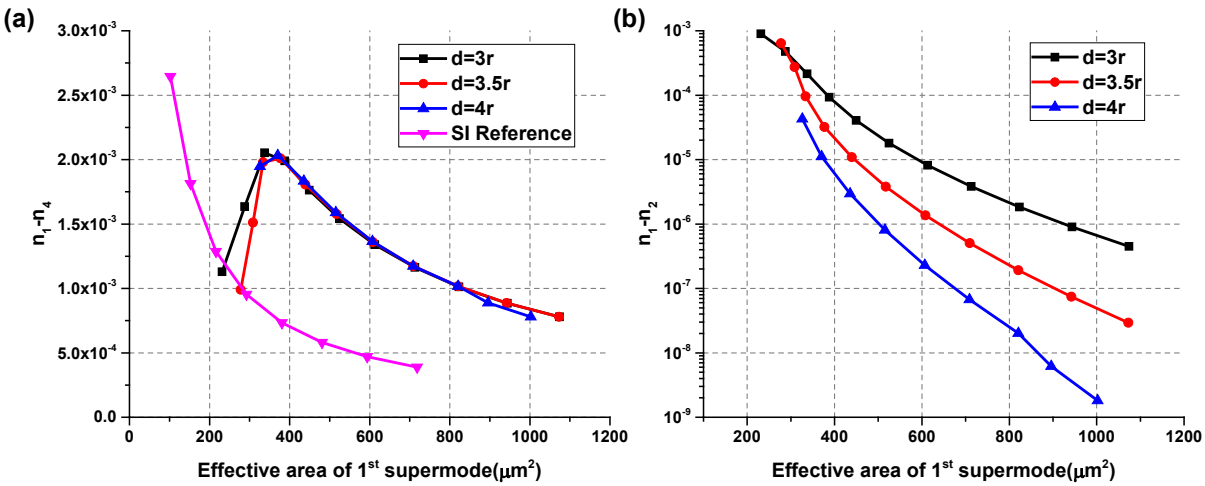

Figure 6: (a) Effective index difference of the 1st and 4th supermodes, and (b) Effective index difference of the first two supermodes vs. the effective area of 1st supermode, for different core distances.

For FMFs and MCFs with various index profiles, the multiplication of effective index difference and effective area cannot bypass the limit. However, in a 3-core MCF, if the first 3 supermodes have similar effective indices, the effective index difference between them and the 4th supermode may be larger than that limit, for certain effective area of the 1st supermode. The simulated index differences between the 1st supermode and 4th supermode or 2nd supermode with different core-to-core distances, are plotted in Figure 6(a) and 6(b), respectively. Figure 6(a) shows that the multiplication of effective index difference and effective area can be larger than the previous limit. To regard the first 3 supermodes as a mode group, the index difference between them needs to be very small, verified in Figure 6(b). When the core-to-core distance is larger, the index difference between them is smaller, because 3 cores can be regarded more as separate cores, rather than a coupled 'supercore' [49]. The results would benefit the nonlinearity study in fiber transmission system. In this case, both large effective mode area and large effective index difference can be achieved, with the cost of reduced channel number. However, for some

applications like QSM transmission, only one signal channel is needed, so the proposed supermode fibers that break the limit are promising.

CHAPTER THREE: MGM TRANSMISSION IN WEAKLY-COUPLED FMFS

3.1 Low-crosstalk mode multiplexer

In addition to low-crosstalk FMFs, low-crosstalk mode (de)multiplexers are also needed, for MGM transmission, since they combine modes carrying different optical signals in the transmitter side and separate modes in the receiver side, to make sure that fiber can transmit multichannel information effectively. There are two categories of mode multiplexers based on their mechanisms: transverse field profile matched multiplexers and longitudinal propagation constant matched multiplexers.

One multiplexer based on matching longitudinal propagation constants is the fiber-based directional couplers [50, 51]. The mode in SMF can be coupled into the higher-order modes in FMF if their propagation constants are almost the same. However, it is hard to purposely couple SMF mode into one certain degenerate mode in normal directional couplers. One method is to use structured directional coupler pairs to multiplex degenerate modes [52], as shown in Figure 7(a). The bandwidth of directional coupler is also limited.

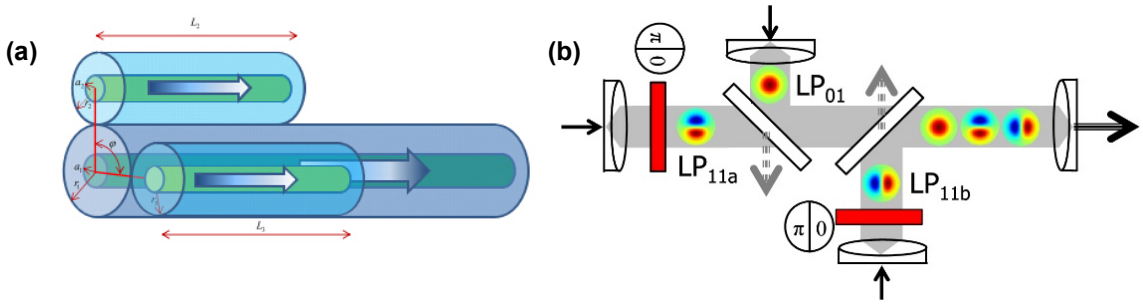

Figure 7: (a) Structured directional coupler for mode MUX, and (b) MDM based on mode conversion in combination with passive combining [14].

Mode multiplexers based on matching transverse mode field profiles, are usually free-space components. The simple one is mode conversion in combination as shown in Figure 7(b). Higher order modes can be converted by fixed phase plates or tunable spatial light modulators (SLMs) by matching spatial phase distribution [53-55]. However, mode conversion combination multiplexers have large loss due to passive combining loss of phase plates or SLMs, as well as coupling loss between free space and fiber.

Spot-based multiplexer is another type of multiplexer based on matching transverse mode field profiles [56]. It directly matches the complex mode profile to several SMFs, the minimum number of which equals to the total number of fiber modes. The insertion loss is smaller without passive combining loss at the beam splitters.

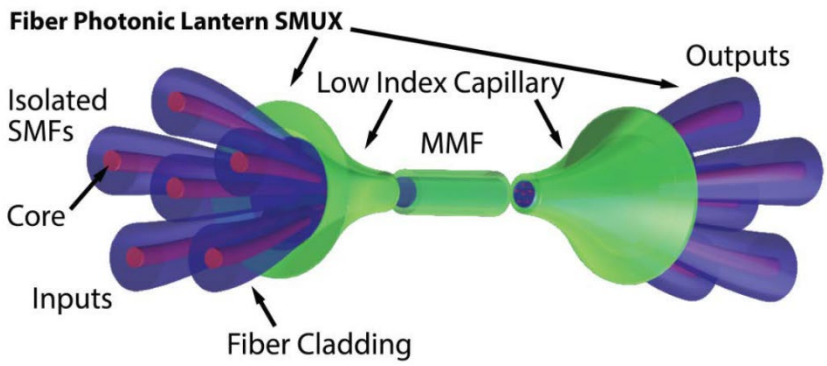

Figure 8: Schematic of photonic lantern [57].

The photonic lantern (PL) is the integrated-optics embodiment of the spot-based coupler, with an adiabatic transition region between SMFs and FMF [57]. A pair of PLs is shown in Figure 8. A PL consists of several SMFs encapsulated inside a low refractive index glass capillary, which is tapered to match the transmission FMF. The mismatch between mode profiles of sparse spots and FMF can be slowly eliminated by the adiabatic tapered transition region. Mode profile of sparse spots from SMFs is first transformed into a supermode of the MCF in the middle stage and

then into the mode profile of the FMF. The ideal PL has a unitary coupling matrix which means no loss of this device. However, the arrangement of cores should be optimized carefully to achieve lossless coupling between SMFs and FMF. The PL can be symmetric or mode (group) selective. In a symmetric PL, the optical power from one input SMF is coupled into different modes in the output FMF since SMFs and cores in the adiabatic transition region are identical all the time. A mode selective PL has dissimilar input fibers and cores in the adiabatic transition region so that each input fiber only launches one mode (group) at the output FMF. In this case, MIMO DSP may be eliminated, together with low-crosstalk FMFs.

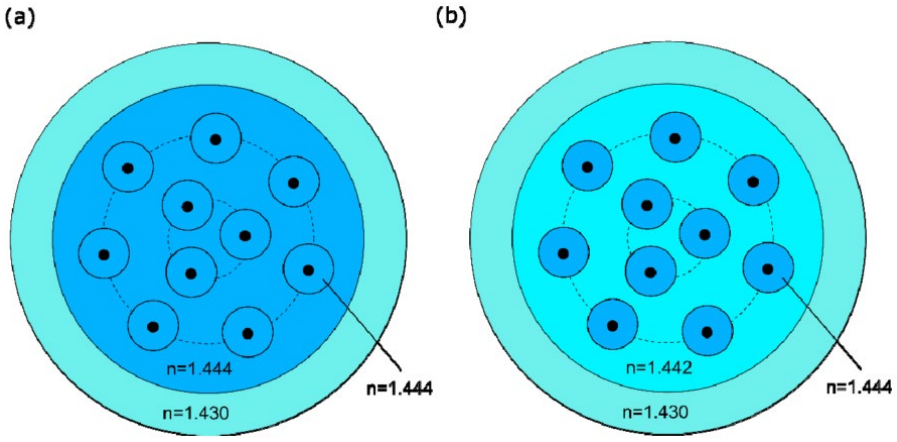

Figure 9: Schematic of micro-structured preform with (a) double-clad PL, and (b) triple clad PL [58].

For the PL supporting more than 6 modes, the fabrication is more complex, since it is harder to place SMFs into the right positions by hand. Using preforms is a method to facilitate the process of PL fabrication. For N modes, the tapering length is proportional to N^2, which also increases the fabrication difficulty. Meanwhile the preforms with larger cladding material would also make the fabrication more complex. Double-clad or triple-clad micro-structured preforms can

alleviate the adiabaticity complexity as shown in Figure 9 [58, 59], since they can reduce the rate of change of mode field, thus decreasing the adiabaticity requirement as shown as

$$\left| \frac{2\pi}{\beta_1 - \beta_2} \int \Psi_1 \frac{\partial \Psi_2}{\partial z} dA \right| \ll 1 \tag{3.1}$$

where β_1, β_2 are propagation constants for two modes, Ψ_1 and Ψ_2 are electrical fields of two modes. When the formula is very small, there is adiabatic mode conversion during the fiber propagation. On the contrary, nonadiabaticity means mode coupling.

3.2 MGM transmission

With low-crosstalk FMFs and mode multiplexers descripted in previous sections, MIMO-less MGM becomes feasible. In FMFs, degenerate modes are easily coupled to each other along transmission [60], so they need to be regarded as one channel and collecting power from all degenerate modes is essential for maintaining stable SNR or bit error ratio (BER). Stable 3x10 Gb/s MGM transmission with direct detection, and the advantages of receiving all degenerate modes in each mode group at the receiver, are demonstrated experimentally here [61]. The SI FMF, which was designed with large effective index difference between mode groups, and low-crosstalk mode-selective PLs as (de)multiplexers used in the work enable a transmission distance of 20 km, much longer than previous MGM transmission demonstrations [62, 63].

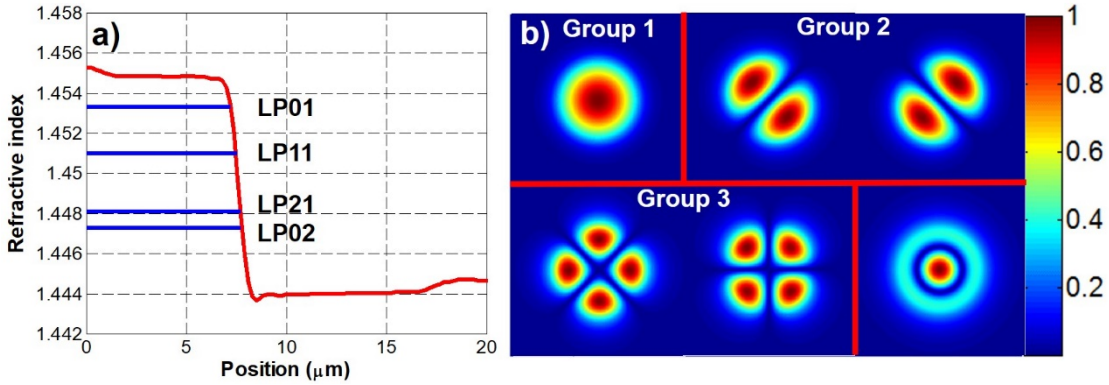

Figure 10: (a) Refractive index profile of FMF, and effective indices of LP modes. (b) Intensity profiles of each of the supported LP modes.

The FMF was specifically designed to increase the effective index difference between the mode groups, reducing coupling between them. The FMF we used in this work supports 6 spatial modes at 1550 nm [64], and we used the first 5 modes as 3 mode groups to perform the transmission experiment. Figure 10(a) shows the index profile and effective indices of all supported modes; the effective index differences between mode groups is $\geq 2.3 \times 10^{-3}$. Simulated mode intensity profiles are also shown in Figure 10(b).

Low-crosstalk mode multiplexer and mode demultiplexer are required to launch and receive different modes in the FMFs. Different components can be used as mode (de)multiplexers, among which the PL is lossless in theory, and has been shown to achieve excellent mode selectivity [65, 66]. A PL consists of several SMFs encapsulated inside a low refractive index glass capillary, which is tapered to match the transmission FMF. SMFs with different core sizes are used to fabricate a mode-selective PL, and the propagation constant of each SMF is matched to that of the corresponding mode in the FMF through an adiabatic taper.

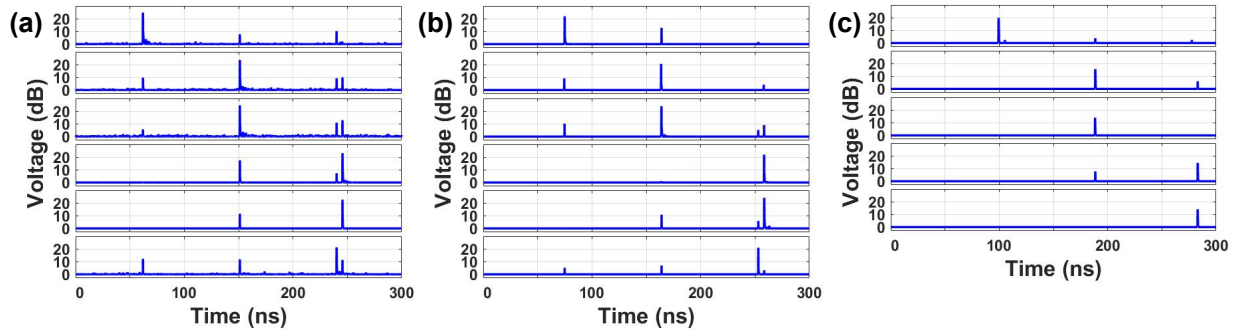

Figure 11: Measured impulse response for (a) PL 1, (b) PL 2, and (c) PL 3. Each PL is spliced to a 20 km FMF.

Three PLs were used in the work: one as the mode multiplexer, the second one as the mode demultiplexer, and the last one as the degenerate mode combiner at the receiver. Impulse responses of the PL spliced with FMF were measured to characterize the mode crosstalk of the PLs and the FMF, shown in Figure 11. A short pulse was launched into one input SMF of each PL to excite one mode in the FMF, and multiple pulses appeared due to mode crosstalk and group delays (GDs). After 20-km propagation, the mode crosstalk could be characterized from the amplitudes of the pulses at different GD times. The first PL has mode-group crosstalk lower than -9 dB at all ports except LP_{21a}, so it was used as the mode multiplexer, and LP_{21b} was used as the input port for LP_{21} group transmission. The second PL has mode-group crosstalk lower than -9 dB at all ports, and it was used as the mode demultiplexer. The third PL has 5 working ports and mode-group crosstalk lower than -6.5 dB, which was used as the degenerate mode combiner after the mode demultiplexer.

Stable 3x10 Gb/s MGM transmission with direct detection was demonstrated using the setup shown in Figure 12. A 10 Gb/s data stream of length 2^{31}-1 was split into three paths and decorrelated with different time delays. Each signal was connected to one SMF of the multiplexer PL to excite the corresponding mode group. After propagation through the 20-km FMF, the MGM signal was demultiplexed by the second PL. LP_{01} mode is directly detected by a receiver for BER

measurement, while two degenerate LP_{11} and LP_{21} modes are combined through the third PL to be detected by the receiver. The propagation delays of degenerate modes were compensated by adjusting the length difference of input SMFs between the second and third PLs.

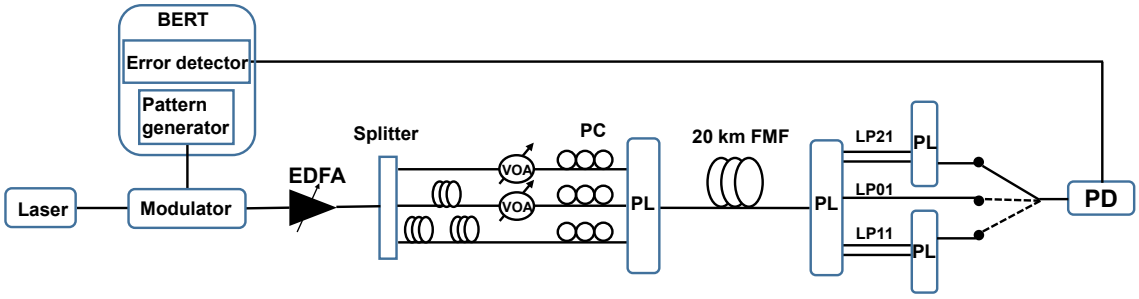

Figure 12: Experiment setup for MGM transmission. BERT: bit error ratio tester; EDFA: erbium-doped fiber amplifier; VOA: variable optical attenuator; PC: polarization controller; PL: photonic lantern; PD: photodetector.

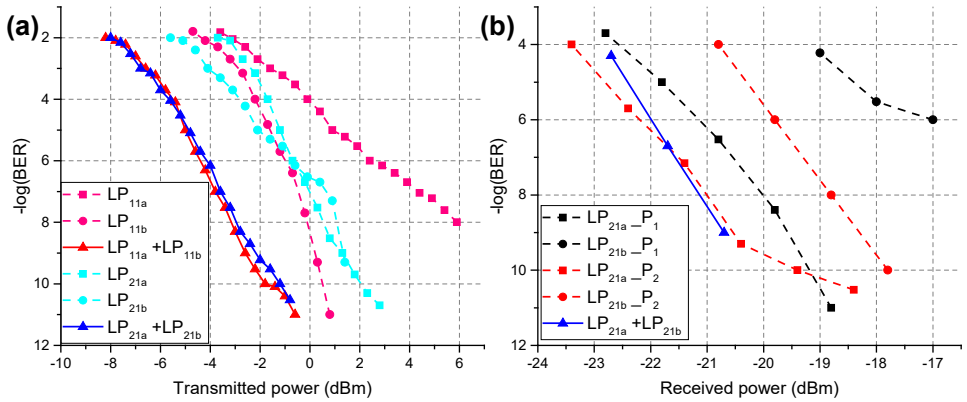

Figure 13: (a) Measured BERs as functions of transmitted power for detecting only one of degenerate modes or both degenerate modes of the LP11 and LP21 group. (b) Measured BERs as functions of received power for detecting only one of degenerate modes or both degenerate modes of the LP21 group for two different transmitting laser polarizations.

Before presenting the results of 3-mode-group transmission, the advantages of combining degenerate modes are first shown in Figure 13. Figure 13(a) plots the BERs as functions of transmitted power for receiving only one or both degenerate modes of LP_{11} or LP_{21} mode group. It shows, as expected, that combining degenerate modes can improve the sensitivity by about 3 dB. In addition, combing degenerate modes can also alleviate polarization fluctuations. As shown in

Figure 13(b), as the polarization of the transmitter laser changes, there is always one degenerate mode with large power penalty, while combing degenerate modes removes this power penalty.

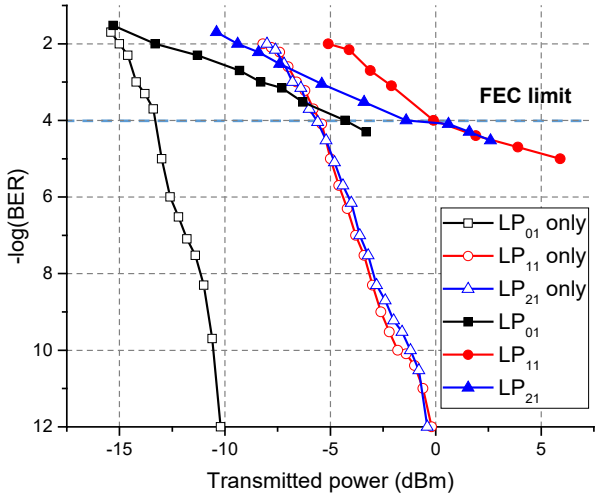

Figure 14: Measured BERs as functions of transmitted power for 3 mode groups. Open symbols represent separate mode-group transmission, and solid symbols represent MGM transmission.

Figure 14 plots the measured BERs when each mode group was separately transmitted or simultaneously transmitted. BERs below 10^{-12} could be achieved for separate transmission of each mode group. There is about a 10 dB power penalty between LP_{01} and LP_{11} or LP_{21}, mainly due to mode-dependent loss (MDL) of the FMF and PLs. Variable optical attenuators (VOAs) were used to equalize the BERs of the three mode groups in MGM transmission. The measured BERs for MGM transmission were worse due to mode crosstalk in the FMF and the PLs, but can still reach the threshold for 7% FEC. Better PLs or other mode multiplexers with lower modal crosstalk are expected to improve the performance further.

CHAPTER FOUR: MODE COUPLING IN FREE SPACE WITHOUT MODAL DISPERSION

In most cases, mode coupling is unavoidable. When there is almost no modal dispersion and only one signal channel, collecting the power of all modes can improve the receiver sensitivity. That's the case in FSO. FSO communication offers an orders-of-magnitude increase in transmission capacity compared to that of the radio-frequency technology. Unfortunately, atmospheric turbulence distorts the wavefront, resulting in spatiotemporal amplitude and phase fluctuations at the detector [67]. Current FSO communication is dominated by the use of adaptive optics (AO) to correct wavefront distortions, followed by single-mode (SM) optically pre-amplified receivers, as shown in Figure 15(a). If the wavefront correction is perfect, such a system can restore the ideal receiver sensitivity at 38.3 photons/bit for on-off keying (OOK) modulation [46]. However, AO FSO systems are expensive and have large size, weight, as well as power consumption. Yet, AO FSO systems still leave much to be desired in terms of performance and reliability. The splitting loss for wavefront sensing dictates that the above theoretical sensitivity limit cannot be achieved in practice. Furthermore, a single AO cannot correct both phase and amplitude distortions associated with moderate and strong turbulence. Since reliability is the key to widespread adoption of FSO communication, it is highly desirable to develop alternative approaches to combat turbulence and improve FSO reliability [68].

Figure 15(b) illustrates the schematic of our proposal, in which the complicated AO and the SM photodetector are replaced by a few-mode (FM) amplifier, which became available very recently due to advances in SDM, and the FM photodetector, respectively [69, 70]. The incoming distorted wavefront can be decomposed into the fundamental Gaussian mode and high-order

modes; the stronger the turbulence the more spatial modes. Fibers with larger numerical apertures (NAs) and/or larger cores can reduce coupling loss, so the signal contained in the distorted wavefront can be received in its entirety by a FM photodiode without pre-amplification. However, such a receiver would lose advantages of optical pre-amplification. Specifically, the sensitivity of receivers based solely on a FM photodiode will be thermal noise limited while that of an optical pre-amplified receiver will instead be limited by noises associated with amplified spontaneous emission (ASE). For SM OOK receivers, the thermal noise-limited sensitivity is >6000 photons/bit while the signal-ASE beat noise-limited sensitivity is 38.3 photons/bit at 10 Gb/s [71]. Therefore, the FM pre-amplifier in Figure 15(b) is essential for constructing a simplified receiver while maintaining high sensitivity.

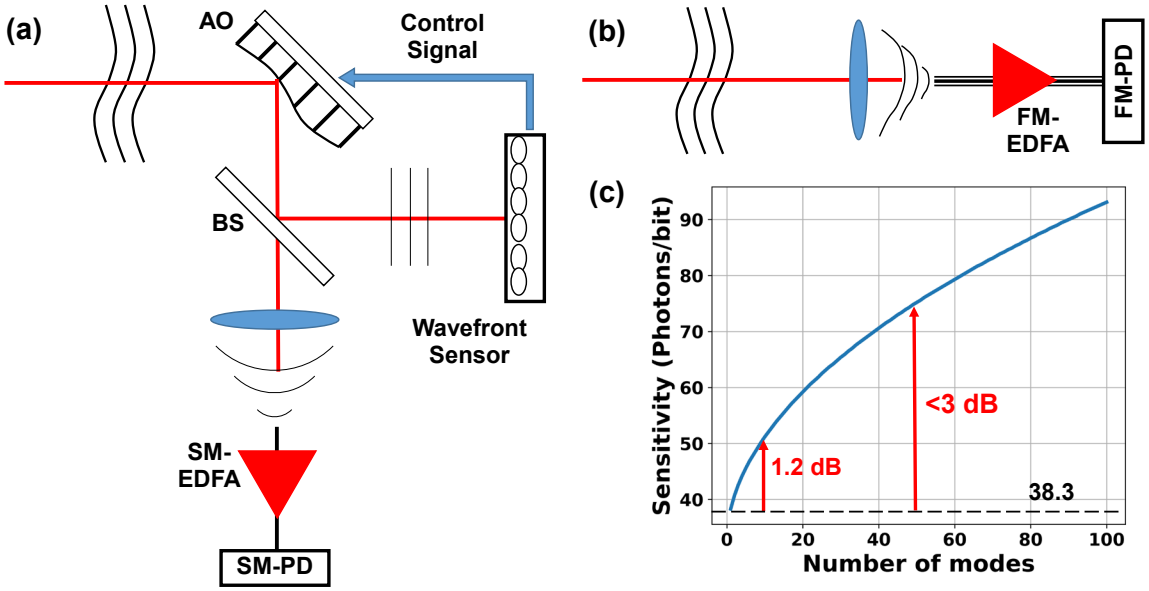

Figure 15: Schematic of FSO using (a) adaptive optics, (b) a FM pre-amplified receiver with (c) its sensitivity as a function of the number of modes.

4.1 Noise statistics and sensitivity of FM pre-amplified PD

We first obtain the sensitivity of FM pre-amplified receivers based on the noise statistics of the photocurrent. For a FM pre-amplified photodetector, the total optical signal can be written as

$$S(x,y,\mathrm{t}) = \sum_{m=1}^{M} E_{v_0,m}\psi_m(x,y)e^{j2\pi v_0 t + j\theta_m} \tag{4.1}$$

where M is the number of modes received by the detector, $E_{v_0,m}$ is the optical field amplitude for mode m in the signal, $\psi_m(x,y)$ is the mode profile of mode m, v_0 is the optical frequency, and θ_m is the phase of mode m. Similarly, the total noise can be written as

$$e(x,y,\mathrm{t}) = \sum_{m=1}^{M} C_{v_0,m}\psi_m(x,y)\,\mathrm{e}^{j2\pi v_0 t} \tag{4.2}$$

where $C_{v_0,m}$ is the optical field amplitude of the noise in mode m. Assuming that the electrical filter following square-law photodetection is an ideal integrate and dump circuit, the decision voltage is given by [71, 72]

$$v(\mathrm{t}) = \frac{1}{T}\int_0^T \iint dxdy\left|S(x,y,t)+e(x,y,t)\right|^2 dt \tag{3.3}$$

where T is the bit period (or the symbol period for multilevel modulation formats). Since all the mode components are orthogonal to each other, the decision voltage in Equation (4.3) can be written as

$$\begin{aligned} v(\mathrm{t}) &= \sum_{m=1}^{M}\mathrm{E}_{v_0,m}^2 + \sum_{m=1}^{M}C_{rv_0,m}^2 + \sum_{m=1}^{M}C_{iv_0,m}^2 + 2\sum_{m=1}^{M}\mathrm{E}_{v_0,m}\,C_{rv_0,m} \\ &= \sum_{m=1}^{M}\left(\mathrm{E}_{v_0,m}+C_{rv_0,m}\right)^2 + \sum_{m=1}^{M}C_{iv_0,m}^2 \end{aligned} \tag{4.4}$$

where $C_{rv_0,m}$ and $C_{iv_0,m}$ are the in-phase (real) and quadrature (imaginary) noise components in mode m, which are zero-mean independent Gaussian random variables with a variance equal to noise power in mode m. Assuming that the photon number in each mode is the same, the decision voltage obeys the noncentral chi-squared distribution [73], with variance $\sigma^2 = n_{sp} h\upsilon G / T$, noncentrality parameter $m_c^2 = \sum_{m=1}^{M} \mathrm{E}_{v_0,m}^2 = \frac{4 n_p h\upsilon G}{T}$, and degree of freedom $n = 2pM$ ($p = 1$ when polarization filtering is used, otherwise $p = 2$), where n_{sp} is the population inversion factor ($n_{sp} \geq 1$) of the optical amplifier, n_p is the average received photon number per bit period, h is the Planck constant, and G is the gain of the amplifier, which is assumed to be the same for all modes.

The probability density function (pdf) of noncentral chi-squared distribution is given by [73]

$$P(x/n, \sigma^2, m_c^2) = \frac{1}{2\sigma^2} \left(\frac{x}{m_c^2} \right)^{n/4-0.5} \exp\left(-\frac{x + m_c^2}{2\sigma^2} \right) I_{n/2-1} \left(\frac{\sqrt{m_c^2 x}}{\sigma^2} \right) \tag{4.5}$$

where $I_{n/2-1}$ denotes the modified Bessel function of order $n/2-1$. After normalization, the variance is $\sigma^2 = n_{sp}$ and the noncentrality parameter is $m_c^2 = 4n_p$. Thus, the decision voltage of the '1' and '0' bits with polarization filtering can be written as $P_1(x/2M, n_{sp}, 4n_p)$ and $P_0(x/2M, n_{sp}, 0)$. The BER of intensity modulation with direct-detection (IMDD) is given by [71]

$$BER = \frac{1}{2} \left(\int_0^{x_{\mathrm{thre}}} P_1(\mathrm{x})\, \mathrm{dx} + \int_{x_{\mathrm{thre}}}^{\infty} P_0(\mathrm{x})\, \mathrm{dx} \right) \tag{4.6}$$

where the decision threshold x_{thre} is determined by equating $P_1(x_{\text{thre}}) = P_0(x_{\text{thre}})$. The BER as a function of the received photon number per bit can be plot numerically, thus the sensitivity for achieving a certain BER can be obtained. Figure 15(c) shows the sensitivity at a BER of 1×10^{-9} as a function of the number of modes.

For SM pre-amplified receivers, signal-ASE beat noise dominates over ASE-ASE beat noise. As the number of modes supported by the FM amplifier increases to accommodate moderate and stronger turbulence, the contribution of ASE-ASE beat noises increases even though the signal-ASE beat noise for a fixed total signal power is independent of the number of modes due to orthogonality of spatial modes. Nevertheless, as can be seen from Figure 15(c), the sensitivity increases sub-linearly with the number of modes. The reason is that as the required number of photons/bit increases with the number of modes in the receiver, signal-ASE beat noise continues to dominate over ASE-ASE beast noise in the FM pre-amplified receivers. As a result, the sensitivity of a 50-mode (moderate turbulence) pre-amplified receiver has a sensitivity of 75 photons/bit, which represents a <3 dB penalty compared to an ideal SM pre-amplified receiver.

In the analysis above, we also assume that the gain for each mode is the same. Optimally, a FM pre-amplified receiver should adjust the gain of each mode to be proportional to the power contained in that mode, similar to the principle of maximum-ratio combining [74]. However, this would entail a complicated amplifier design and control mechanism, which is counter to the desire for simplicity and reliability. In the experiments to follow, we take the approach of ensuring equalized modal gain to balance sensitivity, simplicity and reliability.

4.2 FSO experiment

We now describe our experimental results of FSO communication using the proposed FM pre-amplified receiver, in comparison with a SM pre-amplified receiver without AO, through an FSO channel with turbulence satisfying the Kolmogorov distribution. The schematic of the 10-mode cladding-pumped EDFA used in the experiment, shown in Figure 16(a), has an Er-doped fiber (EDF) of core diameter 26 µm which can support 42 spatial modes for equalizing the gain of the 10 lowest-order modes [75]. The FM EDF has an outer cladding with lower refractive index and an inner cladding with higher refractive index. Pump light coming from a multi-mode laser diode (MMLD) is coupled into the inner cladding of the EDF using side pumping. To do so, we spliced the MMF pigtail of the MMLD to a coreless fiber and down tapered the coreless fiber from 125 µm to 20 µm in a tapering length of 30 mm. At a pump power of 6.6 W, the average small-signal gain of the amplifier is 15 dB and the mode dependent gain (MDG) is less than 2 dB.

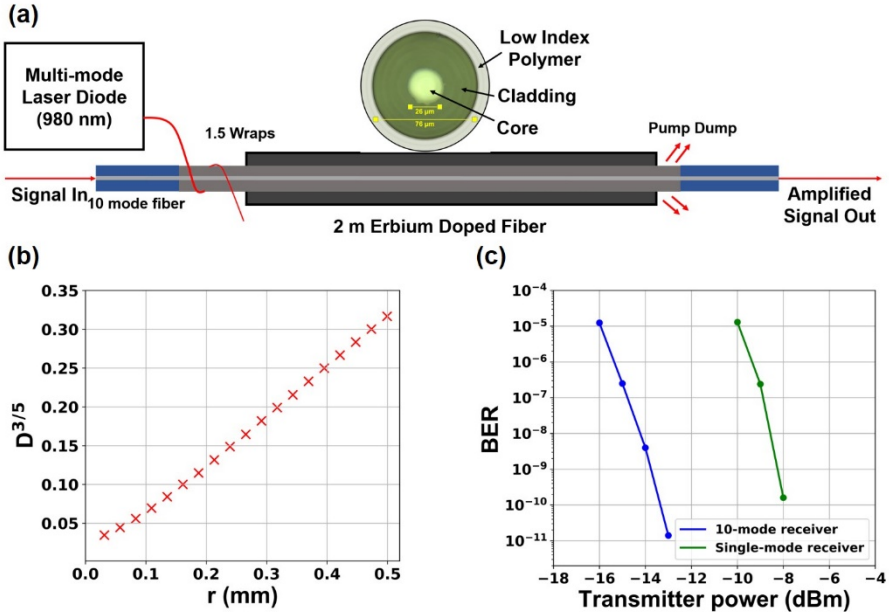

Figure 16: (a) Schematic of the FM preamplifier. (b) Phase function of the phase plate emulating turbulence. (c) Measured BERs as functions of transmitter power for SM and FM pre-amplified receivers.

To emulate turbulence with a Kolmogorov distribution, we fabricated phase plates by repeatedly spray-coating glass substrates with acrylic [76, 77]. We measured the phase structure function $D(r)=\left\langle\left(\varphi\left(\vec{r'}\right)-\varphi\left(\vec{r'}+\vec{r}\right)\right)^2\right\rangle$, where φ denotes the local phase, using phase-shifting interferometry, and r is the distance between two phase positions. The Kolmogorov model has the specific form of the phase structure function $D(r)=6.88\left(\frac{r}{r_0}\right)^{5/3}$, where r_0 is the Fired parameter representing the coherence length. We subsequently calculate $D(r)^{3/5}$ as a function of r. The linear relationship shown in Figure 16(b) validates the Kolmogorov distribution of the phase plates. For the phase plate that we used for our FSO experiment, r_0 is calculated to be 5 mm.

A 10 Gb/s OOK signal beam from a SM transmitter is expanded into a diameter d around 1 cm and propagated through the phase plate, resulting in wavefront distortion of approximately ±4π across the beam. BERs were measured at different transmitter powers as shown in Figure 16(c). The results indicate that the 10-mode pre-amplified receiver provided a 6 dB gain in power budget over the SM pre-amplified receiver.

We now present the statistical property of the receivers based on simulations. In Figure 17(a) we plot the coupling losses of the SM and FM receivers as functions of d/r_0 for a fixed beam diameter of 1 cm, where different d/r_0 values represent different turbulence levels. At each d/r_0 value, we generate 200 wavefront distortions that follow the Kolmogorov model. The shaded region represents the standard deviation of power fluctuation for different realizations of each turbulence condition. It is observed that the average loss and received power fluctuation for the 10-mode receiver are much smaller than those for the SM receiver. In Figure 17(b), we combined

the results in Figures 15(c) and 17(a) to plot the gain in power budget for the FM pre-amplified receiver over that of the SM pre-amplified receiver as a function of the number of modes. The power budget for each case is set to ensure that the probability that the received power is below the sensitivity of the receiver is less than a desired outage probability. Based on the limited number of statistically realizations used in our simulation, we set the outage probability to 15.9%, that is, the received power is at most one standard deviation below the mean. As the number of modes increases, the (standard deviation of) received power (decreases) increases, which improves system performance. In the meantime, the receiver noise (sensitivity) increases (deteriorates). These two opposing dependences result in the existence of an optimum number of modes for each turbulence level.

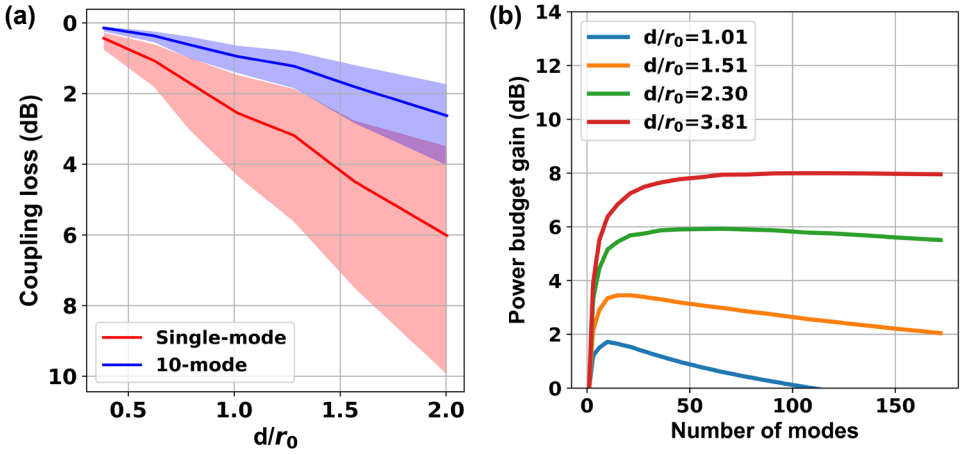

Figure 17: (a) Coupling loss of a distorted wavefront into a SM and FM fiber, as a function of d/r_0 and (b) Power budget gain of FM over SM pre-amplified receiver as a function of the number of modes.

4.3 Comparison with adaptive optics

As shown in previous section, FM pre-amplified receivers can increase the link power budget despite a penalty in received sensitivity as compared to that of SM pre-amplified receivers.

This is because FM pre-amplified receivers can reduce the coupling loss to a larger degree than the penalty in sensitivity. As mentioned previously, adaptive optics is widely used to compensate wavefront distortions. It would be informative to compare the coupling efficiencies of distorted wavefronts into a FM pre-amplified receiver without AO and a SM pre-amplified receiver with AO. As shown in Figure 15, a lens is used to focus the free-space beam onto the facet of the fiber, and the focal length of the lens or the magnification of the imaging system affects the coupling efficiency [78]. For coupling a uniform field into the fiber, an optimum magnification can be calculated [79], which was adopted when simulating the performance of AO. When the turbulence level increases, the number of spatial modes contained in the distorted wavefront and in the receiving FMF also increase. In the meantime, the effective areas of free-space modes and fiber modes scale differently. As a result, an optimum magnification exists for coupling a certain number of free-space modes into the receiving FMF. For the results presented below, an optimum magnification corresponding to the number of free-space modes was used for simulating the performance of the FM pre-amplified receiver. This is reasonable because FSO systems will be designed for the worst-case scenario, i.e., the largest number of modes.

For AO based on deformable mirrors (DMs), Zernike modes are widely used to decompose the distorted wavefront when the aperture is circularly symmetric [80]. This is because the convergence speed is faster when the Zernike coefficients instead of the entire pixelated data from the wavefront sensor are used to control all DM actuators [81]. So simulating coupling efficiency as a function of the number of corrected Zernike modes is very relevant. The results of coupling efficiency as a function of the number of corrected Zernike modes for SM fiber with AO or the number of fiber modes for the FMF without AO are shown in Figure 18, corresponding to weak,

moderate and strong turbulence, respectively. For AO, we include 1) ideal AO, in which wavefront distortion up to a certain order of Zernike modes are completely corrected, and 2) DM AO using a 12x12 deformable mirror. The input wavefront is generated using the power spectral density for turbulence in Kolmogorov's model [82]:

$$\Phi(\kappa) = 0.023 r_0^{-5/3} \kappa^{-11/3} \tag{4.7}$$

where κ is the spatial frequency. All results in Figure 18 are averaged over 20 realizations with the same d/r_0 values.

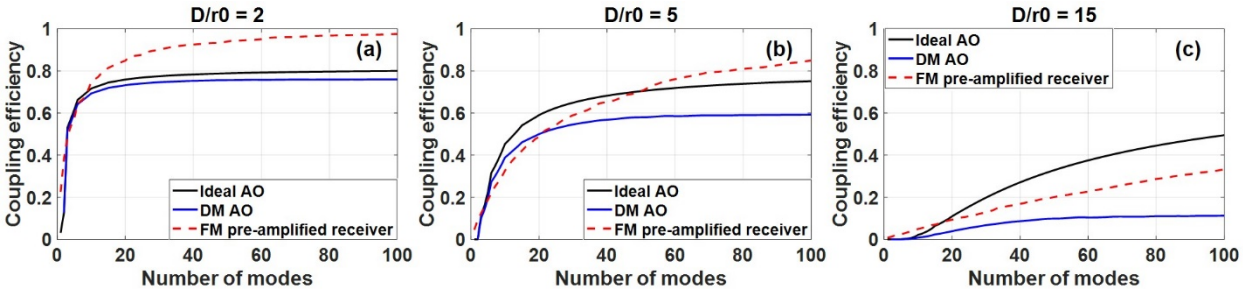

Figure 18: Coupling efficiencies using ideal AO, DM AO, or the FM pre-amplified receiver, with different levels of turbulence for (a) $d/r_0 = 2$; (b) $d/r_0 = 5$; (c) $d/r_0 = 15$. The intensity is assumed to be uniform across the beam.

Under weak atmospheric turbulence ($d/r_0 = 2$) in Figure 18(a), all cases have similar coupling efficiencies for a small number of corrected Zernike modes or fiber modes (N<10). For a larger number of modes, the coupling efficiencies for ideal AO and DM AO have a rather small difference, and FM pre-amplified receiver outperforms AO. Both AO approaches yield similar results because the distorted wavefronts under weak turbulence largely consist of lower-order Zernike modes. Under such conditions, the fitting errors using DM are small. The FM pre-amplified receiver can outperform AO because a superposition of a large number of fiber modes can match the uniform intensity across the beam, in addition to the distorted phase, while AO can only match the phase distortion. Under moderate atmospheric turbulence ($d/r_0 = 5$) in Figure 18(b),

the differences in coupling efficiency between the two AO approaches become larger, since fitting errors for higher-order Zernike modes become larger using DM AO [83]. The FM pre-amplified receiver can outperform ideal AO for a large number of modes (N>40). This is because the mode spectrum in the fiber-mode basis is more spread out compared with Zernike modes. Under strong atmospheric turbulence (d/r_0 =15) in Figure 18(c), the differences in coupling efficiency between ideal AO and DM AO become even larger, and the FM pre-amplified receiver cannot outperform ideal AO. However, for all turbulence levels, the FM pre-amplified receiver can always outperform AO using a 12x12 deformable mirror.

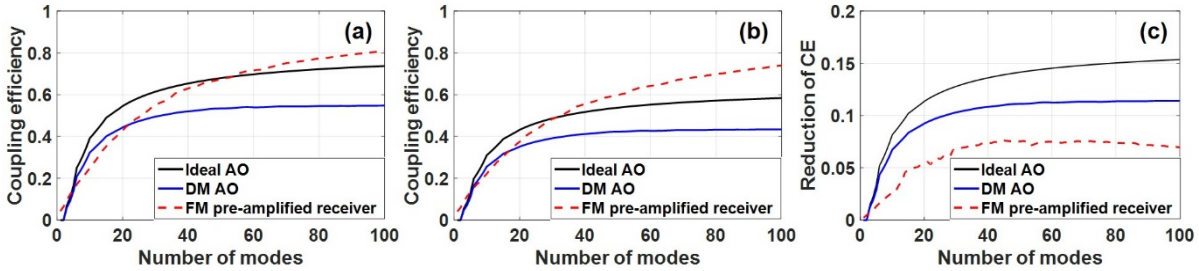

Figure 19: Coupling efficiencies using ideal AO, DM AO, or the FM pre-amplified receiver including (a) the effects of phase distortion only, (b) the effects of both phase and amplitude distortions for an FSO system with a propagation distance of 1 km and C_n^2 value of 10^{-12}. (c) The corresponding reductions in coupling efficiency due to intensity fluctuations across the beam.

The above simulations are based on the assumption that there is only phase distortion, which is only valid for weak atmospheric turbulence [84]. We now include the effect of intensity fluctuation due to strong atmospheric turbulence. In particular, we investigate the effects of turbulence on an FSO system with a range of 1 km and a C_n^2 value of 10^{-12}, which exists frequently near ground in the middle of the day. The Fried parameter r_0 is calculated to be 0.89 cm [76] and the corresponding d/r_0 value is 5.7 for a 2-inch receiving aperture. The intensity

correlation length ρ_0 can be calculated using $\rho_0 = r_0 / 2.1$, which is valid for the high C_n^2 value and scintillation index [85].

Under the above turbulence condition, the coupling efficiencies as functions of the number of corrected Zernike modes or fiber modes are shown in Figure 19(b). The coupling efficiencies with the same phase distortions but ignoring intensity fluctuations are plotted in Figure 19(a). The reductions in coupling efficiency due to the presence of intensity fluctuation for three cases are also shown in Figure 19(c). The reductions in coupling efficiencies using AO are larger, since AO can only compensate distorted phase while the FM pre-amplified receiver is tolerant to both phase and amplitude distortions.

In addition, perfect wavefront sensing has been assumed in above simulations for AO. However, in practice, the accuracy of Shack-Hartmann wavefront sensors degrades severely for moderate and strong turbulence due to scintillations [86]. Interferometric wavefront sensors are required in this case [82, 87], but are not yet commercially available. Turbulence can also cause beam wandering and associated fluctuations in received signal. An additional pointing and tracking system will be needed for both the FM pre-amplified receiver and the SM receiver with AO [88].

In conclusion, we propose and demonstrate FM pre-amplified receivers for FSO to achieve high sensitivity, simplicity and reliability by taking advantage of recent advances in SDM. In this paper, only results for OOK are presented, but the technique can be easily extended to other direct-detection modulation formats, such as differential phase-shift keying (DPSK). Even though multi-subaperture based digital coherent detection can potentially combat turbulence [89], the implementation is complex and costly. Comparison with adaptive optics using deformable mirrors also shows the coupling-efficiency advantage of the proposed method. The above reasons suggest

that the technique presented here likely represents an advantageous, practical method of combating turbulence in FSO.

CHAPTER FIVE: MODE COUPLING IN MMFS WITH LARGE MODAL DISPERSION

MMFs and long-haul FMFs not only suffer from mode coupling but also large modal dispersion. When there are only one signal channel and simple IMDD like in MMF systems, large modal dispersion will bring inter-symbol interference, deteriorating signal performance. When there are multiple signal channels and coherent modulations, MIMO DSP can compensate the large modal dispersion. However, the DSP complexity is still proportional to the modal dispersion. So in both cases, modal dispersion or GDS needs to be managed and reduced effectively.

5.1 Strong mode coupling in MMFs

So far, several methods for reducing the GDS have been proposed. They include optimizing fiber index profiles [90], akin to dispersion-shifted fibers, and modal group delay compensation [29], akin to chromatic dispersion compensation in SMFs. However, both of these methods are effective only for a small number of modes [91]. The most promising method proposed so far is strong mode coupling [92, 93]. When modes are weakly coupled, the GDS increases linearly with the transmission distance. When modes in an FMF are strongly coupled, the GDS increases with the square root of the transmission distance. This is because each MDM signal would have a nearly equal probability of traveling on different modes averaged over the transmission link. A straightforward approach of introducing strongly mode crosstalk is to use a scrambler sandwiched between a mode multiplexer (MUX) and a mode demultiplexer (DMUX) [94]. This approach not only is expensive but also likely incurs losses much higher than what is required as described below.

Traffic in datacenters has dramatically increased in recent years to constitute a dominant fraction of the overall communication traffic [95]. Within datacenters, transceivers based on 850 nm multi-mode (MM) vertical-cavity surface-emitting lasers (VCSELs) and GRIN MMFs currently represent the lowest-cost solution for short-reach applications. However, as line rates of datacenter traffic increase, VCSEL-based MMF links are increasingly threatened by SMF links so much so that Facebook has decided to eliminate MMFs in its new datacenters. The reasons are twofold. First, high-speed VCSELs, although technically feasible [96], have lower output powers and are expected to be more expensive. Second, perhaps more importantly, high line rates call for the use of large-bandwidth OM4 fibers, with manually-selected optimized refractive-index profiles [97], which are about 4 times more expensive than SMFs. Several methods have been proposed to reduce the GDS and improve the bandwidth of GRIN MMFs, for example, using dispersion-compensated MMFs [98]. However, all these methods are inflexible and complicated, therefore expensive as well.

Strong mode mixing is another method to reduce the GDS and improve the bandwidth of MMFs [92, 99]. When mode groups in MMFs are strongly coupled, the majority of a signal pulse would have travelled on all mode groups with nearly equal probability, thus reducing GDS due to modal dispersion [30, 100]. The reduction of GDS alleviates inter-symbol interference and thus improves the BER performance at the receiver. Taking advantage of the unique distribution of the effective indices of parabolic GRIN MMFs, we propose to use one uniform LPG with a fixed grating period to achieve strong coupling among all mode groups [101]. The LPGs were placed along the MMF with approximately uniform spacings, leading to reductions in GDS. Theoretically the GDS is proportional to $1/\sqrt{N}$ (where $N-1$ is the number of LPGs) when the total length is

the same [30]. We present experimental results demonstrating the conversion of an OM3 MMF (300 m at 10 Gb/s [102]) to an OM4 MMF (400 m at 10 Gb/s [102]) with a negligible excess loss of 0.2 dB using simple mechanical LPGs. The proposed approach can benefit from more densely populating LPGs along the fiber. These fibers can be easily manufactured by inscribing LPGs concurrent with fiber drawing [103].

5.2 Experimental setup and results

We measured the performance of the MMF fibers using the experimental setup as shown in Figure 20(a). An evaluation board (EVB) was used as the electrical interface for the VCSEL-based MM transceiver. A bit error rate tester (BERT) was used to generate a 10 Gb/s pseudo-random bit stream (PRBS) of length 2^{31}-1 for intensity modulation of the VCSEL transmitter. The output of the VCSEL transmitter was connected to the spool of MMF. The output from the MMF fiber was fed into the receiving port of the transceiver which was connected to 1) the BERT to measure the BERs, and 2) an oscilloscope to measure eye diagrams. Several segments of fibers were extracted out through re-spooling to allow the application of the LPGs. The MMF in this work is a commercial OM3 fiber of length 300 m (the reach specification of OM3 fibers at 10 Gb/s) or longer. The LPGs were placed along the MMF with approximately uniform spacings. The spacings between 2 LPGs and the ends of 400 m-long (530 m-long) MMFs were 120, 120, 160 m (180, 160, 190 m); The spacings between 4 LPGs and the ends of 400 m-long (530 m-long) MMFs were 80, 100, 60, 80, 80 m (120, 120, 100, 80, 110 m). Although uniform spacing was preferred, the spacing disparities were the result of lack of control in our re-spooling process. The refractive index profile of the OM3 fiber was measured and plotted in Figure 20(b), along with the calculated

effective indices of the 18 mode groups (black lines) at a wavelength of 850 nm. The GRIN profile and the trench can reduce the GDS and bending loss. The effective index differences between neighboring mode group pairs, and the corresponding phase-matched LPG periods are nearly equal, as shown in Figure 20(c). As a result, a uniform LPG with a fixed grating period can be used to couple all mode groups in the MMF to reduce the GDS. In the current experiment, a mechanical LPG was used, which consists of a replaceable plate with gratings cut into it and an upper flat steel plate. The steel plate has an adjustable screw for applying pressure to the fiber [104]. With increased pressure, the coupling efficiency between neighboring mode groups increases due to increased index contrast of the LPG on the fiber, accompanied by a larger loss due to coupling into cladding modes. Since no pressure monitoring capability was provided by the grating manufacturer, we instead use the pressure-induced insertion loss of the grating(s) to indicate the strength of mode coupling.

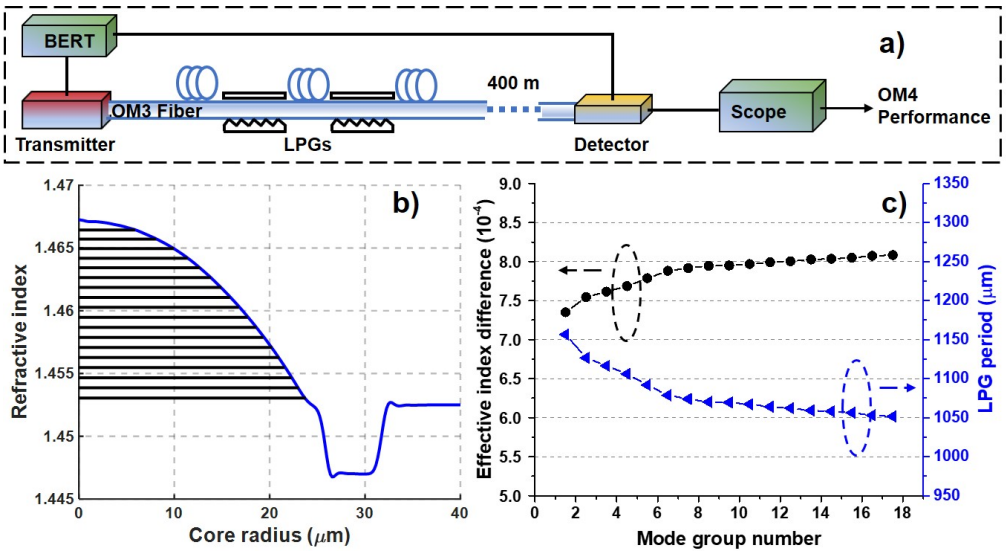

Figure 20: (a) Experimental setup. BERT: bit error rate tester, Scope: oscilloscope, LPG: long-period grating. (b) Measured refractive index profile and calculated effective indices of the 18 mode groups of the OM3 MMF at a wavelength of 850 nm. (c) Computed effective index differences between neighboring mode group pairs, and corresponding phase-matched LPG periods at a wavelength of 850 nm.

The native 300 m OM3 MMF can indeed support error-free transmission at 10 Gb/s, meeting the specification for OM3 fibers. However, when the length of the native OM3 MMF was increased to 400 m, BER increased to around 10^{-8}; the corresponding eye diagram is shown in Figure 21(a). Therefore, the bandwidth of the native OM3 MMF is between 3000 and 4000 $MHz*km$. After 2 mechanical LPGs were applied, error-free transmission was restored on the 400 m OM3 MMF; the corresponding eye diagram is shown in Figure 21(b), revealing appreciable improvement over that in Figure 21(a). Similarly, the BER for transmission over a 530 m native OM3 MMF is around 10^{-3} but can be restored to error free with the application of 4 LPGs, revealing an improved bandwidth larger than 5300 $MHz*km$ with the help of LPGs; the corresponding eye diagrams are shown in Figures 21(c) and 21(d), respectively.

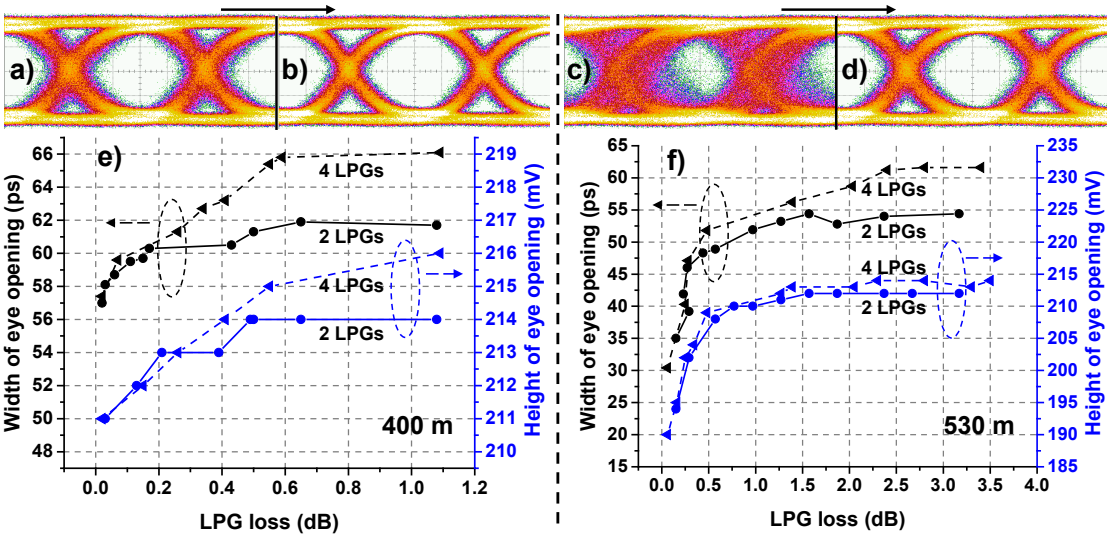

Figure 21: Eye diagrams (a) without LPGs and (b) with 2 LPGs, for 400 m MMF. Eye diagrams (c) without LPGs and (d) with 4 LPGs, for 530 m MMF. The width and height of eye openings as functions of the LPG-induced loss, for (e) 400 m MMF and (f) 530 m MMF.

The eye diagrams in Figure 21 also show that the GDS can be greatly reduced with the help of LPGs. The width or height of eye openings can be used to infer the GDS of the MMFs. Larger GDSs would increase the temporal variance of rising and trailing edges, leading to smaller widths

or heights of eye openings. Figure 21(e) shows that the widths and heights of eye openings increase as the loss induced by LPGs, and thus mode coupling, increase when 2 LPGs and 4 LPGs were applied on the 400 m MMF. Compared with 2 LPGs, 4 LPGs can achieve the same width or height of eye openings with smaller losses. This is expected as more LPGs would curtail modal group delay more effectively. Similarly for the 530 m long OM3 MMF, as shown in Figure 21(f), the width of eye opening can be improved by nearly twofold using either 2 LPGs or 4 LPGs.

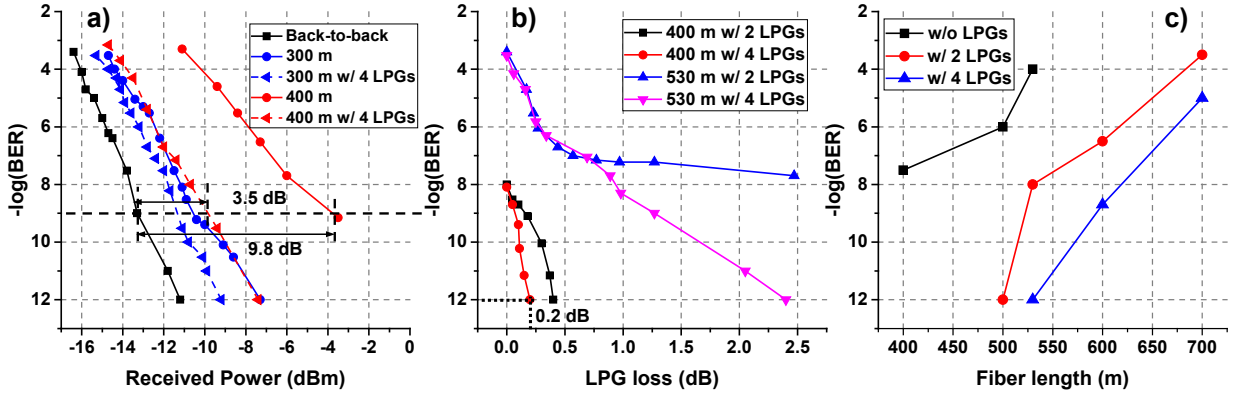

Figure 22: (a) BER as a function of the received power for back-to-back, 300 m (without or with LPGs) and 400 m MMFs (without or with LPGs). (b) BER as a function of the loss induced by LPGs, for 400 m MMF and 530 m MMF. (c) BERs for different lengths of MMF, without, and with 2 or 4 LPGs.

The BER of the signal received by the transceiver was also measured using a BERT. We first measured the back-to-back BER vs. received power as a reference. The BER performances at 300 and 400 m transmission with and without applying LPGs are plotted together with the back-to-back BER in Figure 22(a). It can be seen that the modal dispersion-induced power penalty at 10^{-9} BER for the 400 m transmission is about 9.8 dB and error-free transmission was not possible. When 4 LPGs are applied, the above modal dispersion-induced power penalty was reduced to about 3.5 dB.

The BERs as functions of the total losses incurred by the LPGs to reduce the modal dispersion-induced power penalty are shown in Figure 22(b) at transmission distances of 400 and 530 m with the transmitter power fixed at -1.5 dBm. The BER after 400 m MMF can be easily improved to below 10^{-12} using LPGs with a total loss smaller than 0.2 dB; using 4 LPGs can better improve the BER with smaller loss compared with using 2 LPGs. Similarly, for 530 MMF, 4 LPGs can improve the BER to below 10^{-12} with a loss of 2.4 dB loss. To achieve error-free transmission at 530 m, 4 LPGs must be used. The reason why 2 LPGs cannot achieve error-free transmission is that GDS of mode groups in the MMF was accumulated over too long a distance before mode groups are scrambled. Figure 22(c) compares the BERs as functions of the fiber length when 2 LPGs or 4 LPGs are used with the transmitter power also fixed at -1.5 dBm.

It is important to confirm that performance improvements are indeed due to grating-induced mode mixing, rather than due to mode filtering. The best way to do this is encircle flux testing to measure the mode power distribution. Due to lack of the equipment, we performed two additional tests to verify the cause of performance improvements. First, we used fiber bendings as mode strippers on the MMF and observed the resulting changes in the eye diagram and BER. Both the eye diagram and BER deteriorated with bending. Second, if the performance improvements using the LPG were due to pressure-induced mode filtering, the performance would be independent of the grating period. To this end, we changed the angle between the MMF and LPG from the optimum position and observed deteriorations in the eye diagram and BER. Based on the two tests above, we deduce that mode mixing is the cause of GDS reduction.

5.3 Fabrication tolerance

Our method of converting OM3 to OM4 MMFs takes advantage of the nearly equal effective index differences between neighboring mode group pairs in GRIN MMFs. The effective index differences obviously depend on the refractive index profiles of these fibers, as does modal dispersion. For our method to be attractive, the tolerance on refractive index profiles must be less stringent than for OM4 fibers.

For a GRIN fiber with a core index distribution, as shown in Figure 23(a), satisfying $n^2 = n_1^2 - 2n_1^2\Delta\left(r/a\right)^\alpha$ (where $\Delta = n_1^2 - n_2^2/2n_1^2$, n_1 and n_2 are the refractive indices of the core and cladding, r is the radial position, and a is the core radius), the α value is an important factor determining the effective index differences between neighboring mode group pairs. An index trench is usually added to reduce bending loss. Here we fix the width and the depth of the index trench at 5 μm and 5.5×10^{-3}, respectively, but vary the position of the trench and investigate how this position affects the effective index difference. First, we discuss the effect of the core index profile. Figure 23(b) plots the effective index differences between neighboring mode group pairs at a wavelength of 850 nm for different values of α with a trench immediately outside the core, which is the case for existing OM4 MMFs. As can be seen, for the optimum value $\alpha_{opt} = 1.97$, the effective index difference is almost a constant between all neighboring mode group pairs, while the effective index difference either decreases or increases with mode order when $\alpha < 1.97$ or $\alpha > 1.97$. Specifically, for $\alpha = 1.9$ ($\alpha = 2.1$), the range of effective index differences between neighboring mode group pairs from mode group 1 to mode group 18 is about 4.3×10^{-5} (6.8×10^{-5}). The black curve in Figure 23(c) shows the range of effective index differences or

corresponding matched LPG periods as a function of α for GRIN profiles of existing MMFs [black curve in Figure 23(a)]. It is important to determine the range of α for which our method of using uniform LPGs to reduce modal GDS works efficiently, and to compare that range with what is required for OM4 fibers. As a reference, the tolerance on α for conventional OM4 fibers is around 0.02 [105, 106].

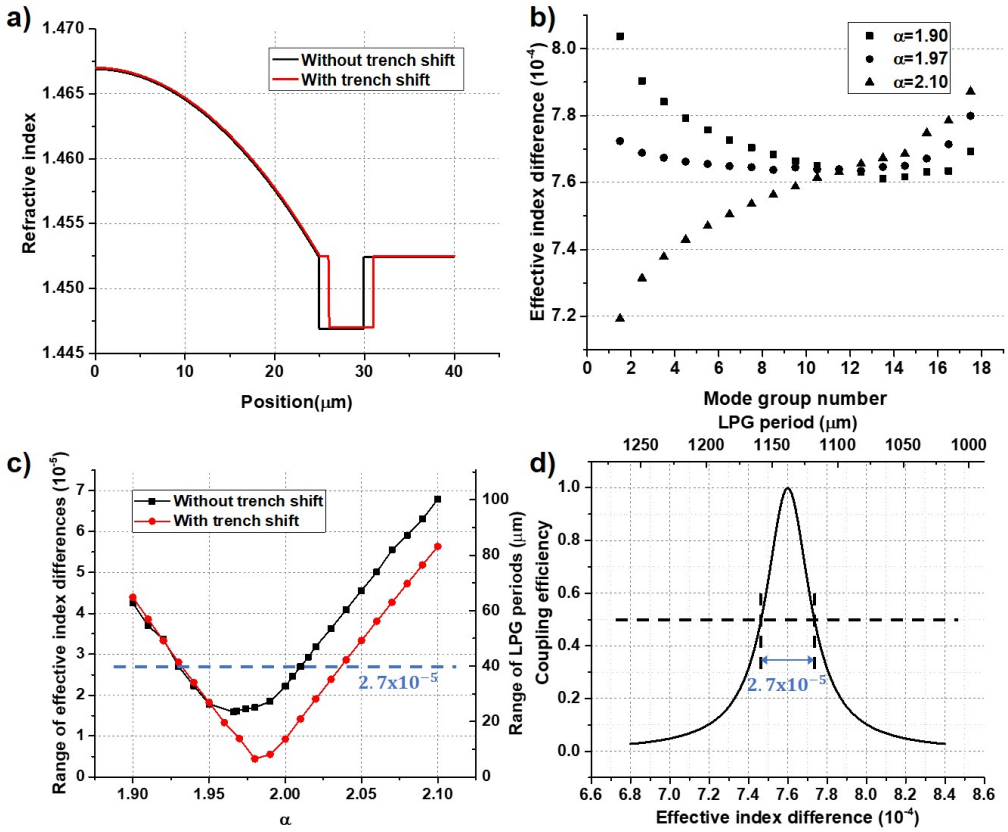

Figure 23: (a) Refractive index profiles without or with trench shift. (b) Effective index differences between neighboring mode group pairs for 3 different α values, for the index profile without trench shift. (c) Range of effective index differences or corresponding matched LPG periods as a function of the α value, without or with trench shift. (d) Coupling efficiency between two modes, as a function of effective index difference or corresponding matched LPG period, for $\kappa = 50/m$, with perfect phase-matched index difference at 7.6×10^{-4}.

Next, we present the effect of the position of the index trench. To reduce the range of effective index differences, we varied the position of the trench and found that shifting the trench

away from the core by 1 μm yields the smallest range of effective index differences or corresponding matched LPG periods, as shown in the red curve in Figure 23(c). It was found that shifting the trench away from the core can reduce the effective index differences between higher-order mode group pairs.

The fabrication tolerance of α depends on the acceptable range of effective index differences or corresponding matched LPG periods, which in turn depends on the coupling coefficient κ. Figure 23(d) plots the coupling efficiency between two modes as a function of the effective index difference or corresponding matched LPG period for a coupling coefficient of $\kappa = 50/m$, with perfect phase-matched index difference at 7.6×10^{-4}. This value of coupling coefficient is approximately the same as in our experiment in previous section, and was deduced from the impulse response, which indicated that complete mode coupling occurred over the total coupling length of 3.5 cm for the mechanical grating [45]. To achieve a coupling efficiency >50%, the range of effective index differences must be smaller than 2.7×10^{-5} or the range of LPG periods must be smaller than 40 μm, as shown in Figure 23(d). This range of effective index differences or LPG periods corresponds to a tolerance on α value around 0.11, which is >5 times greater than the tolerance on α for conventional OM4 fibers mentioned above.

In conclusion, we experimentally demonstrate low-cost and low-loss conversion of OM3 MMFs to OM4 MMFs using strong mode mixing by periodically embedding simple LPGs for datacenter applications. OM3 MMFs can be converted to OM4 MMFs with only 0.2 dB loss over 400 m for 10 Gb/s transmission. Error-free transmission at 10 Gb/s can be extended to 530 m if higher losses can be tolerated. The experiment was done using a specific transceiver and on a specific OM3 MMF. So the improvement in bandwidth may be different with a different

transceiver or OM3 MMF. To verify consistent channel performance, additional tests using different transceivers and OM3 MMFs should be conducted. The proposed approach can benefit from more densely populating LPGs along the fiber. These fibers can be easily manufactured by inscribing distributed LPGs concurrent with fiber drawing [103] leading to better performances and lower costs. Better index profile designs can provide a large α fabrication tolerance. Therefore, the approach presented in this paper could potentially extend the longevity of VCSEL-based MMF links for datacenter applications.

CHAPTER SIX: MODE COUPLING IN FMFS WITH LARGE MODAL DISPERSION

The DSP complexity of an MDM system is proportional to the modal group delay of the fiber link. Modal group delay can determine the temporal memory needed in MIMO time domain equalization (TDE), or the fast Fourier transform (FFT) block length in MIMO frequency domain equalization (FDE), of single carrier modulation. The increased DSP complexity can be accepted in short-reach systems, however, the MIMO DSP would bring large cost and energy consumption in long distance fiber communication systems. Thus it is very important to reduce modal group delay by various methods.

Weak mode coupling occurs randomly and parasitically in FMFs, but strong mode coupling must be introduced intentionally. The LPG is one of the most effective structures to promote strong mode coupling. Since mode coupling induced by LPGs is a coherent, phase-matched process, a different grating is required for each pair of modes (or mode groups) [92, 100]. An intrinsic problem with this approach is that any LPG used for mode coupling can also couple the highest-order guided mode (group) to a cladding mode in a phase-matched manner due to the high density of cladding modes. In addition to this intrinsic loss, each LPG also has extrinsic loss due to imperfections in the grating. Therefore, as the dimension of MDM increases, so does the number of LPGs. A large number of LPGs obviously adds complexity and cost, but a more serious drawback is the loss accumulated by each LPG. Because loss has the most direct impact on the capacity of a communication channel and even 0.01 dB/km of loss reduction is being sought for SMFs, the LPG used to induce strong mode coupling must also introduce extremely low losses,

preferably below 0.1 dB, to ensure that the transmission capacity of an MDM system is competitive with parallel SMF transmission systems.

6.1 FMFs with equally-spaced effective indices

As stated previously, since mode coupling mediated by LPGs is a coherent, phase-matched process, a different grating is required for each pair of modes. The only way to couple all mode groups using only one uniform LPG with a fixed grating period is to ensure that the effective indices of the mode groups are designed to be nearly equally spaced. Similar to parabolic quantum wells that allow equally-spaced energy levels, GRIN fibers with a parabolic index distribution are expected to support mode groups with nearly equally-spaced effective indices, from Equation (2.6). The design of FMFs with equally-spaced effective indices is scalable to a larger number of mode groups. As the number of mode groups grows in a parabolic GRIN fiber, the condition for equally-spaced effective indices becomes better satisfied since most of the modes are well confined.

In reality, evanescent fields do exist in the cladding. So, we adopt a nearly parabolic index profile for the core with a low-index trench in order to strongly confine the guided mode to the core. An optimized design is represented by the blue curve in Figure 24(a). We fabricated a GRIN fiber according to this design. The actual index profile of the FMF is represented by the magenta curve in Figure 24(a), along with the calculated effective indices of modes as black lines. With $n_1 = 1.46,\ \Delta = 0.0109,\ a = 16.4\mu m,\ n_{trench} = 1.437$, the five mode groups (9 LP modes) at 1550 nm have almost the same effective-index differences ranging from 2.54×10^{-3} to 2.55×10^{-3} between successive mode groups for reasons explained above [107]. To characterize mode profiles of different mode groups, as shown in Figure 24(b), we employed the spatially- and spectrally-

resolved imaging (S^2) method [108, 109] as shown in Figure 24(c). A camera was used to record output images of the FMF when light of different wavelengths was launched. By using principal component analysis (PCA) and independent component analysis (ICA) [108, 109], we acquired profiles of all 9 LP modes in Figure 24(b).

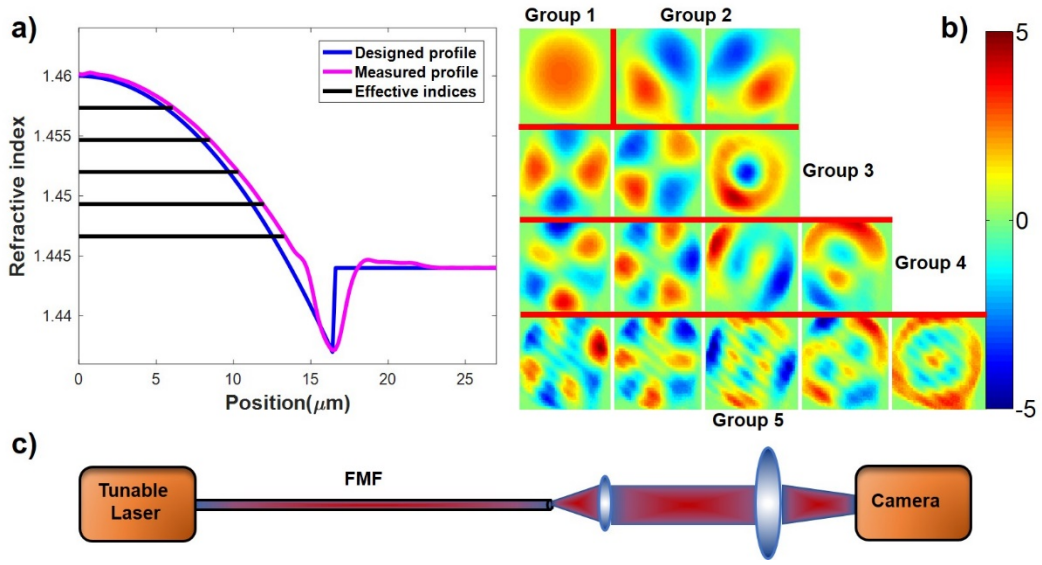

Figure 24: (a) Designed and measured index profiles of FMF, superimposed with calculated effective indices of the 5 mode groups of the measured index profile. (b) Mode profiles measured using the S^2 method. (c) S^2 experiment setup.

6.2 Strong mode coupling and GDS reduction

We first demonstrate enhanced mode coupling among all 9 LP modes using a uniform single-period LPG [45]. Subsequently, we use a series of such LPGs to reduce GDS. Figure 25(a) is the experimental setup for demonstrating strong mode coupling and the reduction of GDS. A data pattern from the pattern generator was used to modulate the light from a laser. The pattern generator produced a short pulse, which consisted of one bit 1 and a long series of bit 0s. After modulation, an impulse of light was launched into one of the input fibers of the PL, which was connected with the GRIN FMF by butt coupling. The 15-mode mode-selective PL made in-house,

although being state-of-the-art, cannot guarantee exciting exactly one mode group at a time. After propagation through the FMF, the signal was detected by a multimode InGaAs PIN+TIA receiver. The receiver was connected to the oscilloscope to record the impulse response waveforms. The pulse generator is Hewlett-Packard 70841B with 3 G bandwidth, the modulator is OKI EAM OM5753C30B with 30 G bandwidth, the receiver is Discovery R402 PIN-TIA with 10 GHz bandwidth, and the oscilloscope is Agilent Infiniium DSO81204A with 12 G bandwidth.

The mechanical LPG consists of a lower replaceable plate with gratings cut into it and an upper flat steel plate over which an adjustable screw is used to apply pressure to the fiber sandwiched between these two plates [104, 110]. This mechanical grating has the same level of uniformity as LPGs fabricated using the arc method [104]. The relative angle between the fiber and the LPG can be adjusted to change the effective grating period.

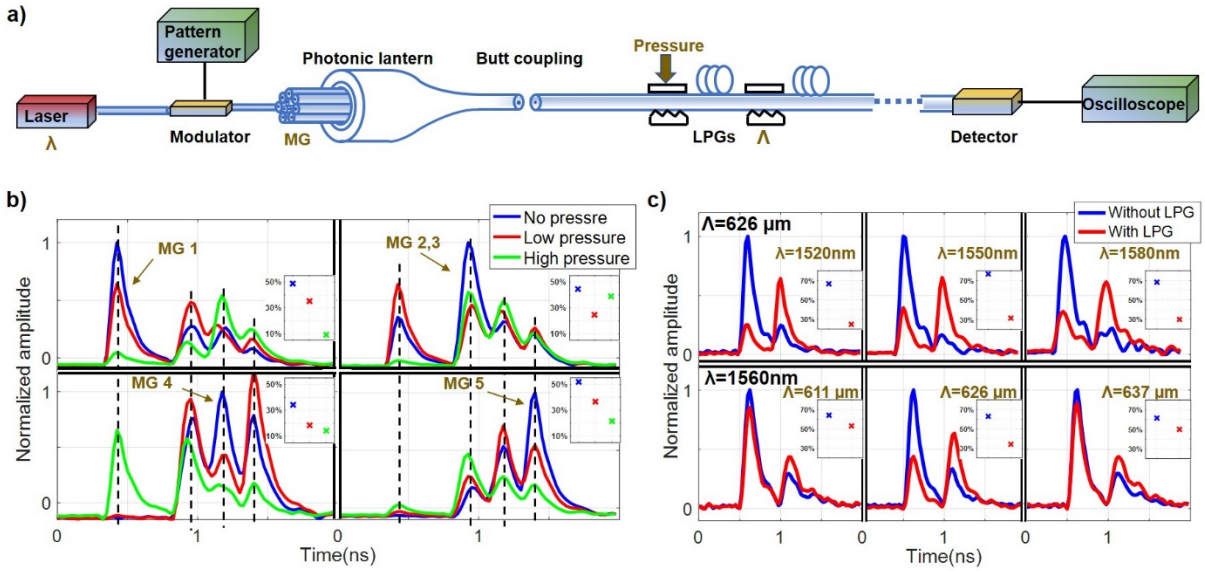

Figure 25: (a) Experimental setup for measuring the impulse response. λ: wavelength of tunable laser, Λ: period of LPGs, MG: mode group. (b) Measured impulse response waveforms with different pressures, when the main power is initially in MG 1, MG 2 and 3, MG 4, MG 5, respectively. (c) Measured impulse response waveforms with and without the LPG for different wavelengths, and for different grating periods. The insets in (b) and (c) show the percentage of power in the dominant input MG for different pressures.

To investigate mode coupling, a single uniform mechanical LPG was applied at the beginning of the FMF. Because of the relatively large effective index difference between mode groups, coupling between mode groups is negligible without the LPG. The PL was used for selective excitation of a dominant mode group when no pressure is applied to the LPG. After applying pressure on the LPG, new modal contents are generated from mode coupling mediated by the LPG. Modal dispersion in the GRIN FMF was exploited to separate different modal groups in the time domain. Therefore, the differences in the powers of each mode group in the impulse responses of the GRIN FMF with and without pressure on the LPG can be used to characterize mode coupling mediated by the LPG. It should be pointed out that, even though the FMF has equally-spaced effective indices, the group indices are, in general, not equally spaced. It turns out that the modal dispersion between the second and third group is rather small for this particular GRIN FMF, so these two mode groups are lumped together. Figure 25(b) demonstrates that a single uniform LPG can indeed induce mode coupling between all mode groups. Taking the top left plot as an example, when no pressure was applied on the mechanical LPG, there was one main peak in the impulse response, representing that the power was mainly in the LP_{01} mode. When pressure was applied on the LPG, more modes/peaks appeared in the waveform, signifying that the power in the LP_{01} mode had been coupled into other mode groups. The red and green lines show the effect of mode coupling as the pressure on the mechanical LPG was successively increased. The inset shows the percentage of power in the dominant input LP_{01} mode for different pressures. It is observed that mode coupling increases with applied pressure. The rest of the plots in Figure 25(b) show the impulse response waveforms when the initial power was mainly in other mode groups. They indicate that power in each mode/peak can always be coupled into not only its

neighboring modes but also next-to-neighbor modes with one LPG. Similarly, the insets show the percentage of power in the dominant input MG for different pressures. When the dominant input is in MGs 2 and 3, the percentage of power in these two groups did not change monotonically with pressure, likely because the power in MG 1 is coupled back into MG 2. It can be concluded that a uniform single-period LPG can couple all the LP modes of the 5 mode groups.

The use of parabolic GRIN fiber also allows the uniform LPGs to achieve strong mode coupling for a broad range of wavelengths. The phase matching condition for coupling between two modes is [111]

$$\frac{\pi \Delta n}{\lambda} = \frac{\pi}{\Lambda}. \tag{6.1}$$

where Δn is the effective index difference between the two modes, λ is the wavelength in free-space, and Λ is the grating period. To evaluate the bandwidth of coupling due to the LPG, effective indices of LP_{01} and LP_{11} at different wavelengths and subsequently, the left-hand side of Equation (6.1), $A_\lambda = \pi \Delta n_\lambda / \lambda$, were calculated. Taking both material dispersion and waveguide dispersion into consideration, the difference in A_λ at 1520 nm and 1580 nm is $r = A_{1580}/A_{1520} - 1 = 3 \times 10^{-4}$, which is small enough to maintain phase matching condition with this wavelength range as shown in the top row of Figure 25(c). The top three plots in Figure 25(c) show that the impulse response waveforms are similar at three different wavelengths, signifying efficient, broadband mode coupling even with a fixed grating. The insets verify that mode coupling is efficient over a broadband. To verify that the broadband coupling was due to the grating rather than simply the applied pressure, the grating period was tuned to observe the change in the impulse-response waveform. As can be seen from the bottom three plots and the three insets in Figure 25(c), mode

coupling is efficient only for certain grating periods that satisfy the phase-matching condition. The grating period only affects the right-hand side $B_\Lambda = \pi/\Lambda$ of Equation (6.1), and the relative difference between the minimum and maximum effective periods is $r = B_{611}/B_{637} - 1 = 4.3\times10^{-2}$ large enough to annihilate the phase matching condition as shown in the bottom row of Figure 25(c). The total insertion loss (IL) when the effective grating period doesn't satisfy the phase matching condition for the guided modes was measured, using the setup in Figure 25, to be less than 0.06 dB. The loss can be considered as the extrinsic non-resonant microbending loss of the LPG.

One of the strengths of the method for enhanced mode coupling proposed here is its scalability to a larger number of modes, including modes with high azimuthal numbers. It should be recognized that what is required is for the mode with a high azimuthal number M (with azimuthal dependence $e^{jM\varphi}$) to couple to its neighbor having an azimuthal number M+1 or M-1 (with azimuthal dependence $e^{j(M+1)\varphi}$ or $e^{j(M-1)\varphi}$). The asymmetry in the grating having a component $e^{\pm j\varphi}$, required to couple modes with a high or low azimuthal number to its neighbor is exactly the same, and independent of M.

We then demonstrate the reduction of GDS using multiple LPGs distributed along the 4.3 km FMF. The lateral offset between the PL and FMF was adjusted to excite all modes at different GDs with almost equal power. For each waveform measured under different pressure/mode-coupling efficiency, the RMS pulse width representing the GDS of the FMF was calculated using the following formula [46]

$$\sigma = \sqrt{\langle t^2 \rangle - \langle t \rangle^2} \tag{6.2}$$

where $\langle t^n \rangle = \frac{1}{N}\int_{-\infty}^{\infty} t^n I(t)dt$, $N = \int_{-\infty}^{\infty} I(t)dt$, and $I(t)$ is the measured intensity waveform. Meanwhile, for each applied force, the loss induced by the LPGs was also measured. The RMS widths as functions of the measured loss induced by two or four LPGs are shown in Figure 26. The insets are the impulse response waveforms at different losses/pressures. At low pressure (low loss), the optical power remained evenly distributed among the 4 peaks. When a strong force was applied on the grating plate, 4 peaks in the impulse response merged into an almost symmetric single peak centered at the average group delay. The RMS width decreased as the average loss/applied pressure increased. As expected, when four LPGs were used along the FMF, the GDS was reduced further compared with using only two LPGs, because GDS was accumulated over a shorter distance before modes are scrambled. Theoretically, the RMS width is proportional to $\sqrt{N}$ ($N-1$ is the number of LPGs) [30] when the length of fiber between two LPGs is the same. Thus when the total length is the same, the RMS width is proportional to $1/\sqrt{N}$. The fluctuations in RMS width and loss are due to environmental changes such as temperature and fiber deformation.

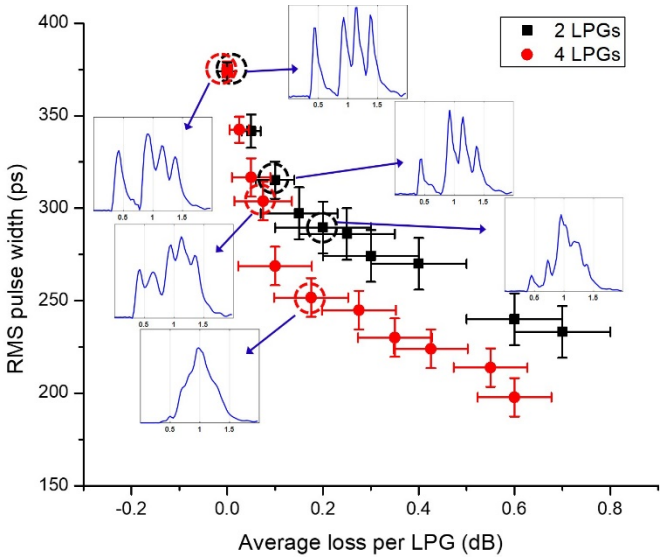

Figure 26: RMS pulse width as a function of average loss per LPG for the cases in which two and four LPGs were used along the 4.3 km FMF. Insets are waveforms corresponding to different losses/pressures for 2 LPGs or 4 LPGs. Horizontal and vertical error bars are calculated from the standard deviation of RMS pulse widths and losses measured under the same condition.

6.3 Reducing intrinsic loss and MDL

We now turn our attention to reducing the intrinsic loss and MDL. We use the RMS of log-unit MDL here, which is the statistically important parameter for characterizing MDL in the strong coupling regime [112]. Figure 26 shows that significant mode mixing can be achieved using LPGs, accompanied by an average loss of 0.6 dB. It is desirable to further reduce this loss. The main source of the loss is due to the seemingly unavoidable power transfer from the highest-order mode group into cladding modes. This also means that the resulting MDL is large. In order to alleviate this problem, we propose the use of a specially designed fiber for the LPG, which supports at least one more mode group than that supported by the fiber for transmission. The rationale is explained in Figure 27 by comparing two different fibers used in the grating section for the same transmission fiber that supports five mode groups. The fiber in Figure 27(a) is a trench-assisted GRIN fiber, and

it supports five mode groups. The index profile is adjusted to make the effective indices of the five mode groups equally spaced to ensure efficient mode coupling, and the use of a trench was found to be necessary. The fiber in Figure 27(b) is a GRIN fiber with a pedestal at the core-cladding boundary, and it supports six mode groups, one more group than that supported by the transmission fiber. The index profile is adjusted to make the effective indices of the first five mode groups equally spaced, and the effective index difference between the fifth and sixth mode groups much smaller than the average index difference between the first five mode groups. Eliminating the trench and adding the index pedestal was found to be necessary. We used the finite-element method (FEM) for the mode solver. The two fibers in Figures 27 (a) and 27(b) have the same core/cladding indices but different radius values of 16.4 μm and 12.75 μm and α values of 2.0 and 1.986, respectively. The pedestal has a width and height of 0.55 μm and 0.0035, respectively.

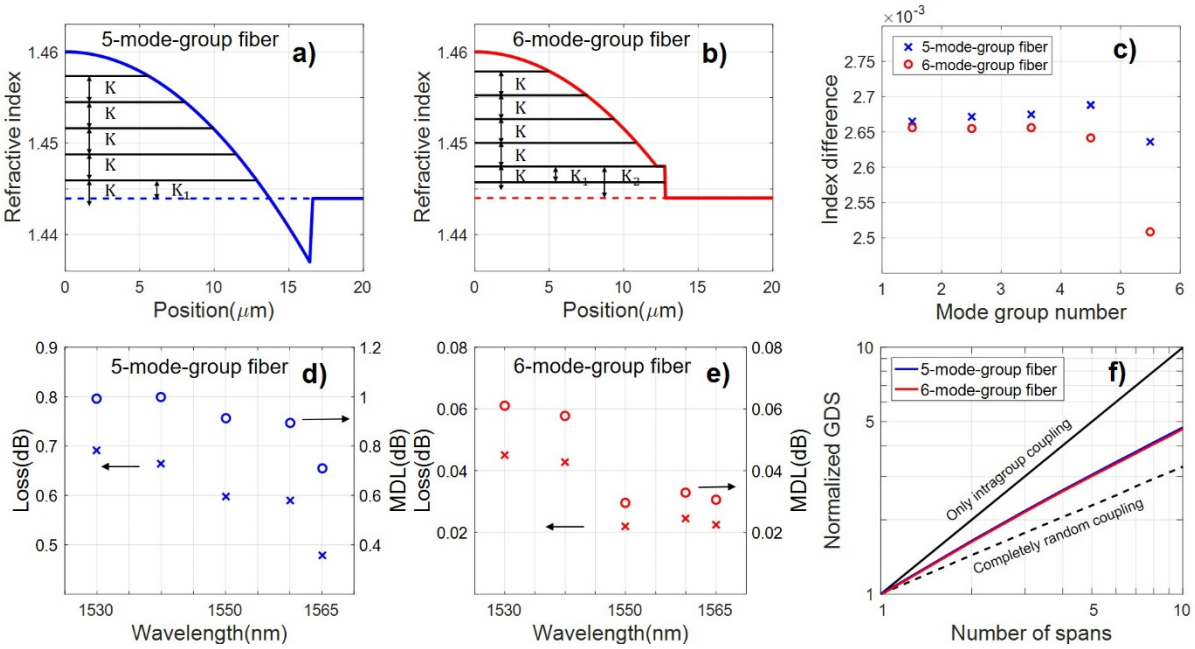

Figure 27: (a), (b) Index profiles of the 5-mode-group fiber and the 6-mode-group fiber. Black lines represent effective indices of each mode group. K is average refractive index difference between two neighboring mode groups that are nearly equally spaced, $K_1 < K < K_2$. (c) Index differences between mode groups in the 5-mode-group fiber and the 6-mode-group fiber,

respectively. The last blue point represents the index difference between the highest-order core mode group and the cladding index. (d), (e) IL and MDL vs. wavelength for LPGs written in the 5-mode-group fiber and the 6-mode-group fiber, respectively. (f) Normalized GDSs as functions of the number of spans using LPGs written in the 5-mode-group fiber and the 6-mode-group fiber, compared with the cases of intragroup coupling and completely random coupling.

The black lines in Figures 27(a) and 27(b) represent the effective indices of mode groups in these two fibers. It can be seen that the effective index difference between the highest-order mode group and the cladding index is always smaller than the average index difference between the neighboring core mode groups for both index profiles. Figure 27(c) plots the effective index differences between neighboring mode groups. The last blue point in Figure 27(c) represents the index difference between the highest core mode group and the cladding index in the 5-mode-group fiber. So, when an LPG phase matched for core mode coupling is applied on the 5-mode-group FMF, the highest-order mode group would be easily coupled to some cladding modes, incurring a large intrinsic loss.

This seemingly unavoidable intrinsic loss can be eliminated using the fiber in Figure 27(b) that supports one more mode group than the 5-mode-group transmission fiber. As can be seen in Figure 27(b), the index difference between the last two mode groups ($K_1=2.51\times10^{-3}$) is much smaller than the average effective index difference between successive core mode groups ($K=2.65\times10^{-3}$) as shown in Figure 27(c), while the effective index difference between the second highest-order mode group and the cladding index ($K_2=2.73\times10^{-3}$) is much larger than K. In this case, it will be inefficient for the first 5 mode groups to couple into either the highest-order mode group or the cladding modes. So when signals are contained in the first 5 mode groups in the 6-group FMF, the intrinsic loss of the LPG can be significantly reduced.

The reduced IL and MDL of the proposed method have been verified by numerical simulations. Our method relies on the properties of the FMF in which the grating is applied, more so than the particular types of gratings that are used. In our simulations here we assume tilted index gratings rather than mechanical gratings were used. We assume that the MDM signal is carried on a transmission fiber that supports 5 mode groups and LPGs are used periodically to enhance mode coupling. LPGs written in a 5-mode-group GRIN FMF and a 6-mode-group GRIN FMF, as described above, are compared. The GDSs for these two cases are computed from the eigenvalues of the group delay operators, which, in turn, are computed from the transfer matrix of the fiber link [113].

To provide a fair comparison of IL and MDL, we adjusted the parameters of the LPGs for these two cases so that the reductions of GDS for these two cases are statistically identical. To do so, we plot the ensemble average of the standard deviations of the group delays, normalized by the group delay of one span for 100 instances of the random intragroup coupling matrices and the span lengths as a function of the number of spans. The nearly identical GDSs for these two cases, as shown in Figure 27(f), were achieved with a grating length of 3.5 cm, tilt angle of 85^{o}, and index contrasts of 5.5×10^{-5} and 6×10^{-5} for the index LPGs written in the 5-mode-group GRIN FMF and a 6-mode-group GRIN FMF, respectively. Tilting is necessary because different spatial modes are orthogonal to each other, and there would be no coupling between different modes without tilting. The GDSs for these two cases increase approximately with the square-root of the number of spans (or propagation length) due to strong mode coupling mediated by both types of LPGs. The GDSs as a function of the number of spans for the case of intragroup coupling only and completely random coupling among all modes are also shown for comparison.

From the coupling matrices of the LPGs used for Figure 27(f), we use singular-value decomposition to compute the IL and MDL as functions of wavelength for the two types of LPGs [112]. Using LPGs in an FMF with the same number (5) of mode groups as the transmission fiber, the IL and MDL are in the 0.6 dB and 1 dB range, as shown in Figure 27(d). On the other hand, using LPGs in an FMF with one more mode group than the transmission fiber, the IL and MDL are reduced to below 0.05 and 0.06 dB respectively, as shown in Figure 27(e). As can be seen, using LPGs in an FMF supporting one more mode group than the transmission fiber significantly reduces the loss and MDL over the entire C band.

In the simulations to demonstrate the reduction of loss using LPGs written on FMFs that support one more mode group, we obtain the transfer matrix of the link by multiplying the propagation matrix, including the effect of random intragroup coupling, of each transmission fiber span and the coupling matrix of each LPG. Completely random coupling between degenerate modes in a mode group, represented by a random unitary matrix, is assumed as this indeed occurs in real fibers. An extra length of fiber uniformly distributed between ± 1m is added to each span to account for the imprecise positions of the LPGs. To obtain the coupling matrix of the LPGs, we first compute the mode profiles of core modes and cladding modes of the GRIN FMFs, and then the coupling coefficients among all modes. Subsequently, we use the coupled-mode equations to calculate the coupling matrix of the LPGs [31, 114, 115] among core modes as well as cladding modes. To ensure the calculated loss is accurate, 4 cladding mode groups are included.

In conclusion, we propose and experimentally demonstrate the reduction of GDS using LPGs with very low insertion loss and mode-dependent loss. By designing an FMF with equally-spaced effective indices on which the LPG is applied, all mode groups in the FMF can be

efficiently coupled using just one uniform LPG with a fixed grating period, instead of a different LPG for each mode group pair. In addition, by applying the LPG in an FMF that supports at least one more mode group than the transmission fiber, insertion loss and mode-dependent loss due to coupling from the core mode to the cladding mode can be largely suppressed. These strategies lead to the lowest intrinsic and extrinsic losses as well as mode-dependent loss to date, for inducing strong mode coupling using LPGs. Furthermore, we have verified that low-loss strong mode coupling could be achieved over a broad range of wavelengths. By periodically applying these LPGs along the transmission fiber, GDS increases as the square root of the transmission distance, rather than linearly without strong mode coupling. These results illustrate that simple LPGs can serve as a practical tool to reduce the GDS in FMFs, thus overcoming the MIMO DSP complexity issue, which is one of the most critical challenges for the practical implementation of mode-division multiplexed systems.

6.4 Strong mode coupling in MCFs

MCFs can be regarded as special FMFs when cores are coupled to each other, since supermodes can be the mode basis of the coupled-core MCFs. Thus, increasing mode coupling is also needed here to reduce DSP complexity. In MCFs, the coupling between cores can be weak or strong depending on the distance between cores. When core distance is large enough, separate cores can carry separate information, which need no DSP MIMO in the system. However, the large core distance can reduce the core density in the cladding area with the limited size, so coupled-core MCFs with smaller core distance attract attention in recent years. In this case, similar to mode crosstalk in FMFs, there is also mode crosstalk in coupled-core MCFs, even when supermodes are

used as the basis. Unlike FMFs or MMFs, the supermodes in MCFs with both bending and twisting, can be different at different positions [116, 117], so the crosstalk between them can be large when the bending radius is small or the twisting rate is large.

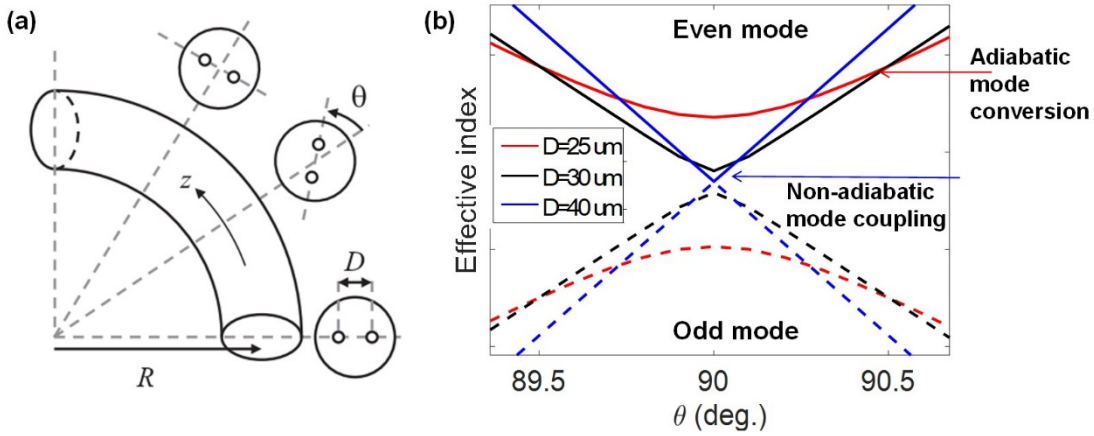

Figure 28: (a) Diagram of bend and twisted 2-core fiber [116]. (b) Diagram of effective index as a function of twist angle for different core pitches.

Figure 28(a) shows the diagram of bend and twisted 2-core fiber, where D is the core distance between two cores, R is the bending radius, and θ is the twisting to bending angle (TBA). There are two supermodes: even mode and odd mode, which have different effective indices, as shown in Figure 28(b). TBA=90 degrees makes the effective index difference between two supermodes minimum. This is the location where most efficient mode coupling occurs, and decreasing core pitch would increase the minimum effective-index difference.

$$\left| \frac{2\pi}{\beta_1 - \beta_2} \int \Psi_1 \frac{\partial \Psi_2}{\partial z} dA \right| \ll 1 \tag{6.3}$$

Equation (6.3) is the adiabatic criterion for the two-supermode MCF [118], where β_1, β_2 are propagation constants of two supermodes, Ψ_1 and Ψ_2 are electrical fields of two supermodes. When the formula is very small, there is adiabatic mode conversion during the fiber propagation,

on the contrary nonadiabaticity means mode coupling. From Equation (6.3) small $\Delta\beta$ and large overlap integral would benefit the mode coupling. In the following, we simulate the adiabatic criterion as a function of TBA for different core pitches. Used parameters are shown as: bending radius $\mathrm{R} = 80\,\mathrm{mm}$, core radius $\mathrm{a} = 4.5\mu\mathrm{m}$, core radius difference $\Delta a = 0.2\mu\mathrm{m}$, index contrast $\Delta = 0.35\%$, working wavelength $\lambda = 1550\,\mathrm{nm}$, and simulation step $\Delta\theta = 0.01^{o}$. First we do the simulation for identical cores, then for different cores with $\Delta a = 0.2\mu\mathrm{m}$.

Figure 29(a) shows the effective index as a function of TBA for different core pitches. Similar to previous explanation, larger core pitch brings smaller effective index difference between two supermodes, which would increase the adiabatic criterion. Figure 29(b) shows the overlap integral as a function of TBA for different core pitches, from which the overlap integral is larger at the TBA of 90 deg., also benefiting the increase of the adiabatic criterion. Taking these two terms into consideration, Figure 29(c) demonstrates the adiabatic condition value as a function of TBA for different core pitches, from which larger core pitch would bring larger adiabatic condition value. However, for larger core pitch, when TBA is away from 90 deg., the adiabatic condition value is smaller, so accumulated adiabatic condition value needs to be calculated, as shown in Figure 29(d). The maximum accumulated value is at the core pitch of $18\,\mu\mathrm{m}$, which means that at the optimized core pitch, the mode coupling is largest, with the same bend radius and twist rate.

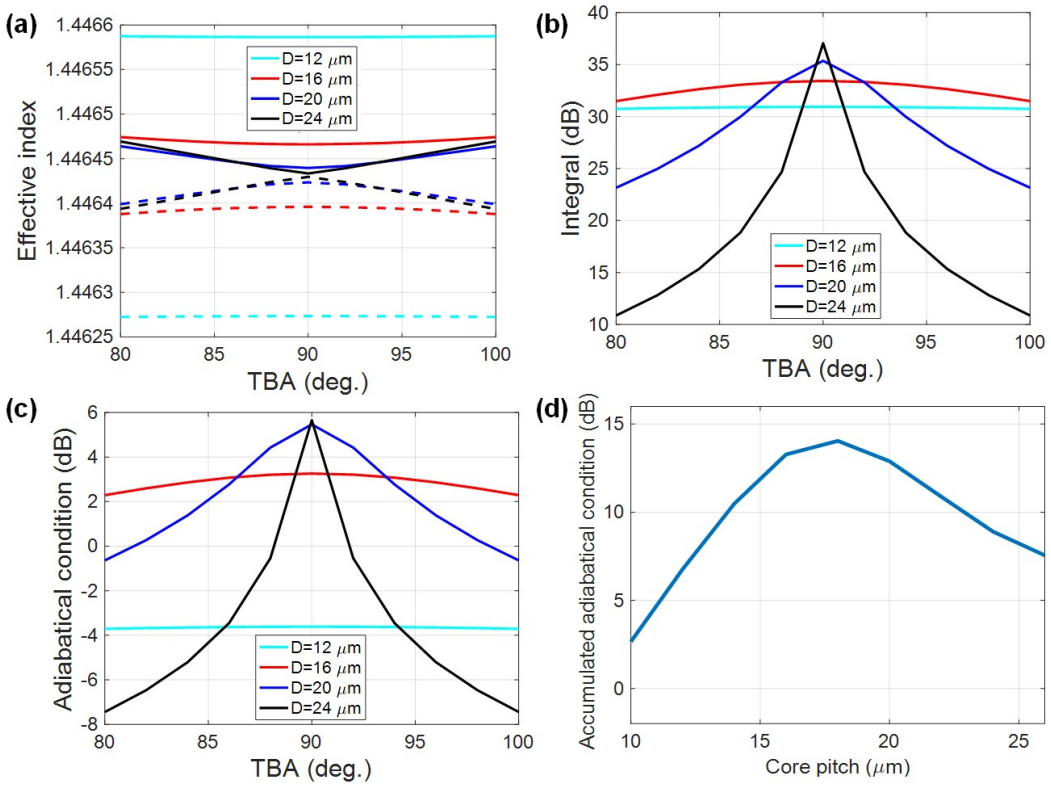

Figure 29: (a) Effective index, (b) overlap integral, (c) adiabatic condition value as a function of TBA for different core pitches, for identical cores. (d) The accumulated adiabatic condition value as a function of the core pitch.

We do the simulation again with different core radiuses $\Delta a = 0.2\mu\text{m}$. Figure 30(a) shows the effective index as a function of TBA for different core pitches. Similarly, larger core pitch brings smaller effective index difference between two supermodes. However, the location of the minimum index difference changes for different core pitches. Figure 30(b) shows the overlap integral as a function of TBA for different core pitches, from which the overlap integral is larger for larger core pitch, which can bring large overlap integral. Taking these two terms into consideration, Figure 30(c) demonstrates the adiabatic condition as a function of TBA for different core pitches. Figure 30(d) shows the accumulated adiabatic condition value as a function of the core pitch, which shows that the mode coupling is largest at the optimized core pitch of 16.25 μm.

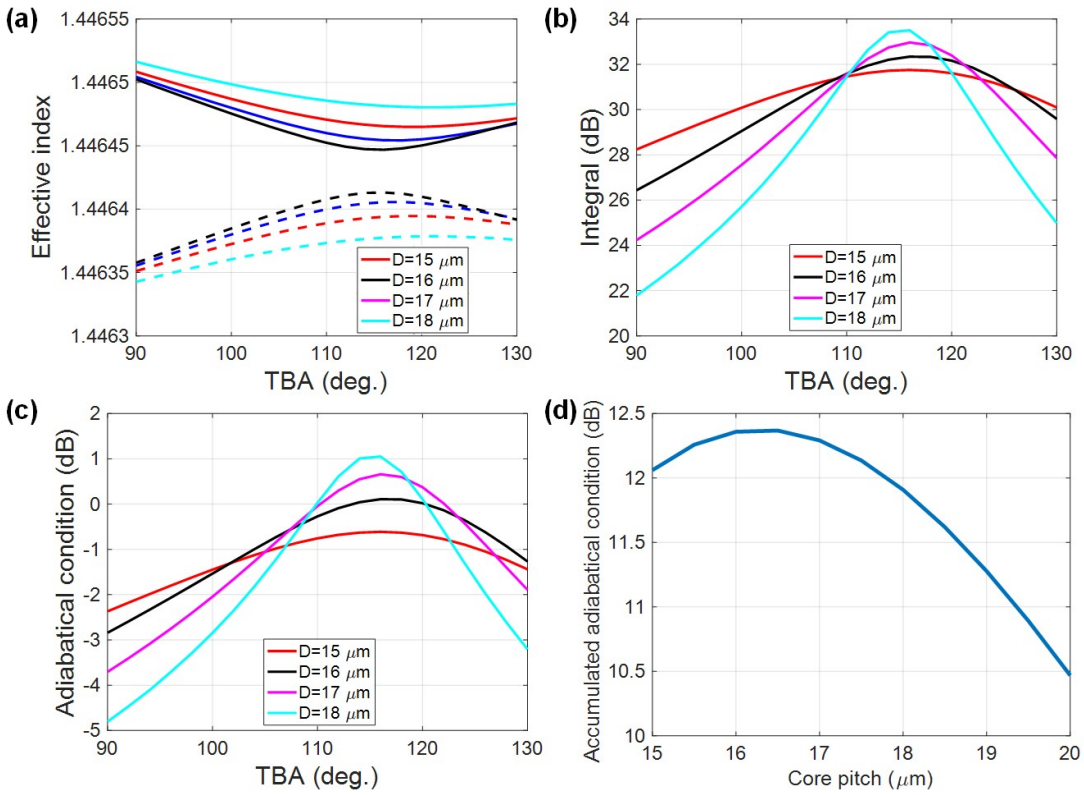

Figure 30: (a) Effective index, (b) overlap integral, (c) adiabatic condition value as a function of TBA for different core pitches, for different cores, with $\Delta a = 0.2\mu\mathrm{m}$. (d) The accumulated adiabatic condition value as a function of the core pitch.

From above simulation results, the optimal core pitch is different for various core differences. To verify that, accumulated adiabatic condition values as functions of core pitches for various core differences, are simulated as shown in Figure 31(a). Similarly, various core sizes, index contrasts and bending radii can also affect the optimal core pitch for mode coupling. The corresponding simulations are done as shown in Figures 31(b)(c)(d). The results show that when core radius difference is larger, core size is smaller, index contrast is larger, or bending radius is smaller, the optimal core pitch is smaller for the best mode coupling. Usually for smaller optimal core pitch, the accumulated adiabatic condition value is smaller. For practical MCF parameter design, those results are helpful to get both stronger mode coupling and larger core density.

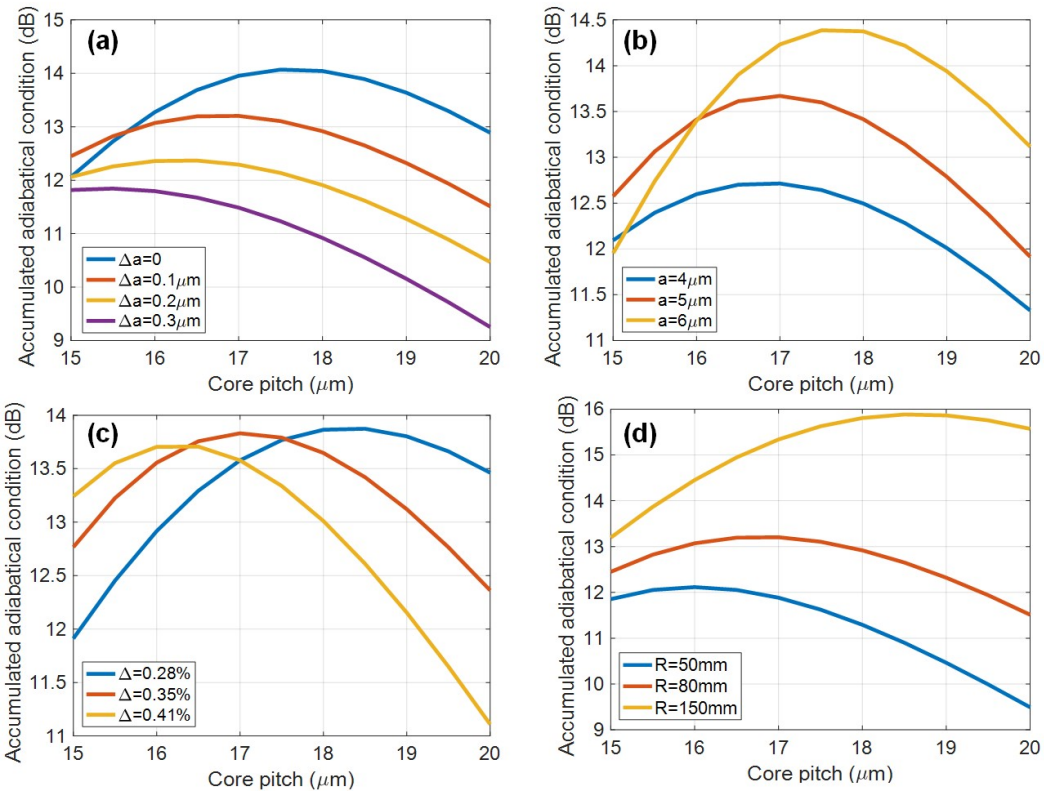

Figure 31: Accumulated adiabatic condition values as functions of core pitch, for (a) various core radius differences, (b) core sizes, (c) index contrasts, (d) bending radii.

CHAPTER SEVEN: CONCLUSION

In this dissertation, we demonstrate different ways to manage the mode coupling in different scenarios. In short-reach fiber systems with a small number of modes, coupling among mode groups can be reduced to be negligible, with large effective index differences between mode groups, eliminating DSP. In most other cases, mode coupling is unavoidable. In FSO communication systems with turbulence, the initial launched fundamental Gaussian mode would be coupled to other modes. Since there is almost no modal dispersion, few-mode pre-amplified receiver can be used to mitigate the effect of turbulence without using adaptive optics. MMFs or long-haul FMFs also suffer from large modal dispersion, which can only be compensated by DSP. Here strong mode coupling is introduced as a counterintuitive approach to reduce modal group delay and DSP complexity. These different ways are summarized as follows:

1. We experimentally demonstrate 3x10 Gb/s mode-group multiplexed transmission over a 20km FMF with large effective index difference between different mode groups, and using photonic lanterns as low-crosstalk mode multiplexer and demultiplexer. OOK modulation and direct detection without MIMO DSP are applied. A third PL is used to combine degenerate LP_{11} or LP_{21} modes to verify the advantages of combining degenerate modes. These results illustrate that mode-group multiplexed transmission with direct detection can play a role in intra-datacenter networks and other short-reach applications.

2. We experimentally demonstrate few-mode pre-amplified receivers to achieve high sensitivity, simplicity and reliability by taking advantages of recent advances in SDM, in FSO communication where there is crosstalk to higher-order modes from fundamental Gaussian mode due to turbulence. Comparison with adaptive optics using deformable mirrors also shows the

coupling-efficiency advantage of the proposed method. The above reasons suggest that the technique presented here likely represents an advantageous, practical method of combating turbulence in FSO.

3. We experimentally demonstrate the reduction of GDS using LPGs with very low insertion loss in graded-index MMFs and FMFs with equally-spaced effective indices, so all mode groups can be efficiently coupled using just one uniform LPG with a fixed grating period. OM3 MMFs can be converted to OM4 MMFs with only 0.2 dB loss over 400 m for 10 Gb/s transmission, and error-free transmission at 10 Gb/s can be extended to 530 m if higher losses can be tolerated, using strong mode mixing by periodically embedding simple LPGs for datacenter applications. Better index profile designs can provide a large α fabrication tolerance. In addition, by applying the LPG in an FMF that supports at least one more mode group than the transmission fiber, insertion loss and mode-dependent loss due to coupling from the core mode to the cladding mode can be largely suppressed. Furthermore, we have verified that low-loss strong mode coupling can be achieved over a broad range of wavelengths. By periodically applying these LPGs along the transmission fiber, GDS increases as the square root of the transmission distance, rather than linearly without strong mode coupling. The strong mode coupling in MCFs is also simulated, with bending and twisting, and the optimal core pitch in different MCFs is calculated.

LIST OF REFERENCES

1. D. Richardson, J. Fini, and L. Nelson, "Space-division multiplexing in optical fibres," Nature Photonics **7**, 354-362 (2013).
2. R. Essiambre and R. W. Tkach, "Capacity Trends and Limits of Optical Communication Networks," Proceedings of the IEEE **100**, 1035-1055 (2012).
3. P. P. Mitra and J. B. Stark, "Nonlinear limits to the information capacity of optical fibre communications," Nature **411**, 1027-1030 (2001).
4. D. Pinnow, T. Rich, F. Ostermayer Jr, and M. DiDomenico Jr, "Fundamental optical attenuation limits in the liquid and glassy state with application to fiber optical waveguide materials," Applied Physics Letters **22**, 527-529 (1973).
5. Y. Yamamoto, Y. Kawaguchi, and M. Hirano, "Low-loss and low-nonlinearity pure-silica-core fiber for C-and L-band broadband transmission," Journal of Lightwave Technology **34**, 321-326 (2016).
6. M. Shimizu, M. Yamada, M. Horiguchi, T. Takeshita, and M. Okayasu, "Erbium-doped fibre amplifiers with an extremely high gain coefficient of 11.0 dB/mW," Electron. Lett **26**, 1641-1643 (1990).
7. E. Desurvire, J. R. Simpson, and P. Becker, "High-gain erbium-doped traveling-wave fiber amplifier," Opt. Lett. **12**, 888-890 (1987).
8. R. J. Mears, L. Reekie, I. Jauncey, and D. N. Payne, "Low-noise erbium-doped fibre amplifier operating at 1.54 μm," Electron. Lett **23**, 1026-1028 (1987).
9. C. A. Brackett, "Dense wavelength division multiplexing networks: Principles and applications," IEEE Journal on Selected Areas in Communications **8**, 948-964 (1990).

10. R. Tkach, A. Chraplyvy, and R. Derosier, "Performance of a WDM network based on stimulated Brillouin scattering," IEEE Photonics Technology Letters **1**, 111-113 (1989).

11. D.-S. Ly-Gagnon, K. Katoh, and K. Kikuchi, "Unrepeated 210-km transmission with coherent detection and digital signal processing of 20-Gb/s QPSK signal," in *Optical Fiber Communication Conference*, (Optical Society of America, 2005), OTuL4.

12. A. H. Gnauck, P. J. Winzer, C. R. Doerr, and L. L. Buhl, "10× 112-Gb/s PDM 16-QAM transmission over 630 km of fiber with 6.2-b/s/Hz spectral efficiency," in *2009 Conference on Optical Fiber Communication-incudes post deadline papers*, (IEEE, 2009), 1-3.

13. P. J. Winzer, "Spatial multiplexing: The next frontier in network capacity scaling," in *Optical Communication (ECOC 2013), 39th European Conference and Exhibition on*, 2013), 1-4.

14. G. Li, N. Bai, N. Zhao, and C. Xia, "Space-division multiplexing: the next frontier in optical communication," Advances in Optics and Photonics **6**, 413-487 (2014).

15. R. Ryf, H. Chen, N. Fontaine, A. Velazquez-Benitez, J. Antonio-Lopez, C. Jin, B. Huang, M. Bigot-Astruc, D. Molin, and F. Achten, "10-mode mode-multiplexed transmission over 125-km single-span multimode fiber," in *2015 European Conference on Optical Communication (ECOC)*, (IEEE, 2015), 1-3.

16. N. Bai, E. Ip, Y.-K. Huang, E. Mateo, F. Yaman, M.-J. Li, S. Bickham, S. Ten, J. Liñares, and C. Montero, "Mode-division multiplexed transmission with inline few-mode fiber amplifier," Optics express **20**, 2668-2680 (2012).

17. B. Puttnam, R. Luís, W. Klaus, J. Sakaguchi, J.-M. D. Mendinueta, Y. Awaji, N. Wada, Y. Tamura, T. Hayashi, and M. Hirano, "2.15 Pb/s transmission using a 22 core homogeneous

single-mode multi-core fiber and wideband optical comb," in *2015 European Conference on Optical Communication (ECOC)*, (IEEE, 2015), 1-3.

18. H. Takara, H. Ono, Y. Abe, H. Masuda, K. Takenaga, S. Matsuo, H. Kubota, K. Shibahara, T. Kobayashi, and Y. Miaymoto, "1000-km 7-core fiber transmission of 10 x 96-Gb/s PDM-16QAM using Raman amplification with 6.5 W per fiber," Optics express **20**, 10100-10105 (2012).
19. B. Zhu, T. Taunay, M. Yan, J. Fini, M. Fishteyn, E. Monberg, and F. Dimarcello, "Seven-core multicore fiber transmissions for passive optical network," Optics Express **18**, 11117-11122 (2010).
20. R. Ryf, J. C. Alvarado, B. Huang, J. Antonio-Lopez, S. H. Chang, N. K. Fontaine, H. Chen, R.-J. Essiambre, E. Burrows, and R. Amezcua-Correa, "Long-distance transmission over coupled-core multicore fiber," in *ECOC 2016-Post Deadline Paper; 42nd European Conference on Optical Communication*, (VDE, 2016), 1-3.
21. S. Randel, M. Magarini, R. Ryf, R.-J. Essiambre, A. Gnauck, P. Winzer, T. Hayashi, T. Taru, and T. Sasaki, "MIMO-based signal processing of spatially multiplexed 112-Gb/s PDM-QPSK signals using strongly-coupled 3-core fiber," in *2011 37th European Conference and Exhibition on Optical Communication*, (IEEE, 2011), 1-3.
22. R. Ryf, N. Fontaine, M. Montoliu, S. Randel, S. Chang, H. Chen, S. Chandrasekhar, A. Gnauck, R.-J. Essiambre, and P. Winzer, "Space-division multiplexed transmission over 3× 3 coupled-core multicore fiber," in *OFC 2014*, (IEEE, 2014), 1-3.
23. D. Marcuse, "Coupled mode theory of round optical fibers," Bell System Technical Journal **52**, 817-842 (1973).

24. L. Su, K. S. Chiang, and C. Lu, "Microbend-induced mode coupling in a graded-index multimode fiber," Appl. Opt. **44**, 7394-7402 (2005).

25. L. Palmieri, "Coupling mechanism in multimode fibers," in *SPIE OPTO*, (International Society for Optics and Photonics, 2013), 90090G-9009.

26. R. Bouziane, P. Milder, R. Koutsoyannis, Y. Benlachtar, J. C. Hoe, M. Püschel, M. Glick, and R. I. Killey, "Design studies for ASIC implementations of 28 GS/s optical QPSK-and 16-QAM-OFDM transceivers," Optics express **19**, 20857-20864 (2011).

27. P. Sillard, D. Molin, M. Bigot-Astruc, H. Maerten, D. Van Ras, and F. Achten, "Low-DMGD 6-LP-mode fiber," in *OFC 2014*, (IEEE, 2014), 1-3.

28. L. Gruner-Nielsen, Y. Sun, J. W. Nicholson, D. Jakobsen, K. G. Jespersen, R. Lingle, and B. Pálsdóttir, "Few mode transmission fiber with low DGD, low mode coupling, and low loss," Journal of Lightwave Technology **30**, 3693-3698 (2012).

29. T. Sakamoto, T. Mori, T. Yamamoto, L. Ma, N. Hanzawa, S. Aozasa, K. Tsujikawa, and S. Tomita, "Transmission over large-core few-mode photonic crystal fiber using distance-independent modal dispersion compensation technique," Optics express **19**, B478-B485 (2011).

30. S. Miller, *Optical fiber telecommunications* (Elsevier, 2012).

31. W.-P. Huang, "Coupled-mode theory for optical waveguides: an overview," Journal of the Optical Society of America A **11**, 963-983 (1994).

32. T. Mori, T. Sakamoto, M. Wada, T. Yamamoto, and F. Yamamoto, "Experimental evaluation of modal crosstalk in two-mode fibre and its impact on optical MIMO

transmission," in *Optical Communication (ECOC), 2014 European Conference on*, (IEEE, 2014), 1-3.

33. R. Maruyama, N. Kuwaki, S. Matsuo, and M. Ohashi, "Experimental investigation of relation between mode-coupling and fiber characteristics in few-mode fibers," in *2015 Optical Fiber Communications Conference and Exhibition (OFC)*, 2015), 1-3.

34. R. Maruyama, N. Kuwaki, S. Matsuo, and M. Ohashi, "Relationship between mode-crosstalk and fiber characteristics in few mode fibers," in *Optical Fiber Communications Conference and Exhibition (OFC), 2016*, (IEEE, 2016), 1-3.

35. D. Marcuse, "Microbending Losses of Single‐Mode, Step‐Index and Multimode, Parabolic‐Index Fibers," Bell Labs Technical Journal **55**, 937-955 (1976).

36. X. Jin and F. P. Payne, "Numerical investigation of microbending loss in optical fibres," Journal of Lightwave Technology **34**, 1247-1253 (2016).

37. D. Donlagic, "A low bending loss multimode fiber transmission system," Optics express **17**, 22081-22095 (2009).

38. R. Olshansky, "Mode coupling effects in graded-index optical fibers," Appl. Opt. **14**, 935-945 (1975).

39. M.-J. Li, X. Chen, A. Liu, S. Gray, J. Wang, D. T. Walton, and L. A. Zenteno, "Limit of effective area for single-mode operation in step-index large mode area laser fibers," Journal of Lightwave Technology **27**, 3010-3016 (2009).

40. N. Broderick, H. Offerhaus, D. Richardson, R. Sammut, J. Caplen, and L. Dong, "Large mode area fibers for high power applications," Optical Fiber Technology **5**, 185-196 (1999).

41. J. M. Fini, "Large mode area fibers with asymmetric bend compensation," Optics Express **19**, 21866-21873 (2011).

42. J. M. Fini, "Bend-resistant design of conventional and microstructure fibers with very large mode area," Optics Express **14**, 69-81 (2006).

43. F. Yaman, E. Mateo, and T. Wang, "Impact of modal crosstalk and multi-path interference on few-mode fiber transmission," in *Optical Fiber Communication Conference*, (Optical Society of America, 2012), OTu1D. 2.

44. T. Hayashi, Y. Tamura, T. Nagashima, K. Yonezawa, T. Taru, K. Igarashi, D. Soma, Y. Wakayama, and T. Tsuritani, "Effective area measurement of few-mode fiber using far field scan technique with Hankel transform generalized for circularly-asymmetric mode," Optics Express **26**, 11137-11146 (2018).

45. H. Liu, H. Wen, B. Huang, R. A. Correa, P. Sillard, H. Chen, Z. Li, and G. Li, "Reducing group delay spread using uniform long-period gratings," Scientific reports **8**, 3882 (2018).

46. G. P. Agrawal, *Fiber-optic communication systems* (John Wiley & Sons, 2012), Vol. 222.

47. P. A. M. Dirac, *The principles of quantum mechanics* (Oxford university press, 1981).

48. D. Marcuse, "Gaussian approximation of the fundamental modes of graded-index fibers," JOSA **68**, 103-109 (1978).

49. C. Xia, M. A. Eftekhar, R. A. Correa, J. E. Antonio-Lopez, A. Schülzgen, D. Christodoulides, and G. Li, "Supermodes in Coupled Multi-Core Waveguide Structures," IEEE Journal of Selected Topics in Quantum Electronics **22**, 196-207 (2016).

50. J. D. Love and N. Riesen, "Mode-selective couplers for few-mode optical fiber networks," Opt. Lett. **37**, 3990-3992 (2012).

51. I. Gasulla and J. M. Kahn, "Performance of Direct-Detection Mode-Group-Division Multiplexing Using Fused Fiber Couplers," Journal of Lightwave Technology **33**, 1748-1760 (2015).

52. H. Bin, X. Cen, G. Matz, B. Neng, and L. Guifang, "Structured directional coupler pair for multiplexing of degenerate modes," in *Optical Fiber Communication Conference and Exposition and the National Fiber Optic Engineers Conference (OFC/NFOEC), 2013*, 2013), 1-3.

53. J. Carpenter and T. D. Wilkinson, "All Optical Mode-Multiplexing Using Holography and Multimode Fiber Couplers," Lightwave Technology, Journal of **30**, 1978-1984 (2012).

54. C. Montero-Orille, V. Moreno, X. Prieto-Blanco, E. F. Mateo, E. Ip, J. Crespo, and J. Liñares, "Ion-exchanged glass binary phase plates for mode-division multiplexing," Appl. Opt. **52**, 2332-2339 (2013).

55. M. Salsi, C. Koebele, D. Sperti, P. Tran, H. Mardoyan, P. Brindel, S. Bigo, A. Boutin, F. Verluise, P. Sillard, M. Bigot-Astruc, L. Provost, and G. Charlet, "Mode-Division Multiplexing of 2 × 100 Gb/s Channels Using an LCOS-Based Spatial Modulator," Journal of Lightwave Technology **30**, 618-623 (2012).

56. R. Ryf, N. K. Fontaine, and R. J. Essiambre, "Spot-Based Mode Couplers for Mode-Multiplexed Transmission in Few-Mode Fiber," IEEE Photon. Technol. Lett. **24**, 1973-1976 (2012).

57. B. Huang, N. K. Fontaine, R. Ryf, B. Guan, S. G. Leon-Saval, R. Shubochkin, Y. Sun, R. Lingle, and G. Li, "All-fiber mode-group-selective photonic lantern using graded-index multimode fibers," Optics express **23**, 224-234 (2015).

58. B. Huang, J. C. A. Zacarias, H. Liu, N. K. Fontaine, H. Chen, R. Ryf, F. Poletti, J. R. Hayes, J. Antonio-Loppez, and J. Zhao, "Triple-clad photonic lanterns for mode scaling," Optics express **26**, 13390-13396 (2018).

59. B. Huang, J. Alvarado-Zacarias, N. K. Fontaine, H. Chen, R. Ryf, F. Poletti, J. R. Hayes, J. Antonio-Lopez, R. Amezcua-Correa, and G. Li, "10-Mode photonic lanterns using low-index micro-structured drilling preforms," in *Optical Fiber Communication Conference*, (Optical Society of America, 2017), Tu3J. 5.

60. C. Antonelli, A. Mecozzi, M. Shtaif, and P. J. Winzer, "Random coupling between groups of degenerate fiber modes in mode multiplexed transmission," Optics express **21**, 9484-9490 (2013).

61. H. Liu, H. Wen, J. C. A. Zacarias, J. E. Antonio-Lopez, N. Wang, P. Sillard, R. A. Correa, and G. Li, "Demonstration of stable 3x10 Gb/s mode group-multiplexed transmission over a 20 km few-mode fiber," in *Optical Fiber Communication Conference*, (Optical Society of America, 2018), W4J. 2.

62. C. Simonneau, A. D'amato, P. Jian, G. Labroille, J.-F. Morizur, and G. Charlet, "4x50Gb/s transmission over 4.4 km of multimode OM2 fiber with direct detection using mode group multiplexing," in *Optical Fiber Communication Conference*, (Optical Society of America, 2016), Tu2J. 3.

63. G. Labroille, P. Jian, L. Garcia, J.-B. Trinel, R. Kassi, L. Bigot, and J.-F. Morizur, "30 Gbit/s Transmission over 1 km of Conventional Multi-mode Fiber using Mode Group Multiplexing with OOK modulation and direct detection," in *Optical Communication (ECOC), 2015 European Conference on*, (IEEE, 2015), 1-3.

64. P. Sillard, M. Astruc, D. Boivin, H. Maerten, and L. Provost, "Few-mode fiber for uncoupled mode-division multiplexing transmissions," in *European Conference and Exposition on Optical Communications*, (Optical Society of America, 2011), Tu. 5. LeCervin. 7.

65. S. G. Leon-Saval, N. K. Fontaine, J. R. Salazar-Gil, B. Ercan, R. Ryf, and J. Bland-Hawthorn, "Mode-selective photonic lanterns for space-division multiplexing," Optics express **22**, 1036-1044 (2014).

66. A. M. Velazquez-Benitez, J. Alvarado, G. Lopez-Galmiche, J. Antonio-Lopez, J. Hernández-Cordero, J. Sanchez-Mondragon, P. Sillard, C. Okonkwo, and R. Amezcua-Correa, "Six mode selective fiber optic spatial multiplexer," Opt. Lett. **40**, 1663-1666 (2015).

67. J. E. Kaufmann, "Performance limits of high-rate space-to-ground optical communications through the turbulent atmospheric channel," in *Free-Space Laser Communication Technologies VII*, (International Society for Optics and Photonics, 1995), 171-183.

68. H. Liu, B. Huang, J. C. A. Zacarias, H. Wen, H. Chen, N. K. Fontaine, R. Ryf, J. E. Antonio-Lopez, R. A. Correa, and G. Li, "Turbulence-Resistant FSO Communication Using a Few-Mode Pre-Amplified Receiver," Scientific Reports **9**, 16247 (2019).

69. B. Huang, C. Carboni, H. Liu, J. C. Alvarado-Zacarias, F. Peng, Y. h. Lee, H. Chen, N. K. Fontaine, R. Ryf, J. E. Antonio-Lopez, R. Amezcua-Correa, and G. Li, "Turbulence-Resistant Free-Space Optical Communication Using Few-Mode Preamplified Receivers," in *2017 European Conference on Optical Communication (ECOC)*, 2017), 1-3.

70. R. Sampson, H. Liu, X. Su, B. Huang, J. C. A. Zacarias, T. Zhan, R. A. Correa, and G. Li, "Turbulence-resistant free-space communication using few-mode pre-amplifiers," in *Next-Generation Optical Communication: Components, Sub-Systems, and Systems VIII*, (International Society for Optics and Photonics, 2019), 1094707.

71. G. P. Agrawal, *Fiber-optic communication systems,* 4th ed. (Wiley, 2010).

72. K. Iizuka, *Elements of Photonics, Volume I: In Free Space and Special Media* (John Wiley & Sons, 2002), Vol. 41.

73. Y. Han and G. Li, "Noise statistics of and BER estimation using demodulated signals for direct detection differential polarization-phase-shift keying," Optics Express **13**, 2761-2766 (2005).

74. T. K. Lo, "Maximum ratio transmission," in *Communications, 1999. ICC'99. 1999 IEEE International Conference on*, (IEEE, 1999), 1310-1314.

75. N. K. Fontaine, B. Huang, H. Chen, C. Jin, B. Ercan, A. Velázquez-Benetez, S. H. Chang, R. Ryf, A. Schülzgen, and J. C. Alvarado, "Multi-mode optical fiber amplifier supporting over 10 spatial modes," in *Optical Fiber Communication Conference*, (Optical Society of America, 2016), Th5A. 4.

76. T. A. Rhoadarmer, "Development of a self-referencing interferometer wavefront sensor," in *Advanced Wavefront Control: Methods, Devices, and Applications II*, (International Society for Optics and Photonics, 2004), 112-127.

77. S. Thomas, "A simple turbulence simulator for adaptive optics," in *Advancements in Adaptive Optics*, (International Society for Optics and Photonics, 2004), 766-774.

78. P. J. Winzer and W. R. Leeb, "Fiber coupling efficiency for random light and its applications to lidar," Opt. Lett. **23**, 986-988 (1998).

79. Y. Wang, H. Xu, D. Li, R. Wang, C. Jin, X. Yin, S. Gao, Q. Mu, L. Xuan, and Z. Cao, "Performance analysis of an adaptive optics system for free-space optics communication through atmospheric turbulence," Scientific Reports **8**, 1124 (2018).

80. R. J. Noll, "Zernike polynomials and atmospheric turbulence," JOsA **66**, 207-211 (1976).

81. A. Jewel, V. Akondi, and B. Vohnsen, "A direct comparison between a MEMS deformable mirror and a liquid crystal spatial light modulator in signal-based wavefront sensing," Journal of the European Optical Society-Rapid publications **8**(2013).

82. T. A. Rhoadarmer and J. R. P. Angel, "Low-cost, broadband static phase plate for generating atmosphericlike turbulence," Appl. Opt. **40**, 2946-2955 (2001).

83. M. Chen, C. Liu, and H. Xian, "Experimental demonstration of single-mode fiber coupling over relatively strong turbulence with adaptive optics," Appl. Opt. **54**, 8722-8726 (2015).

84. X. Zhu and J. M. Kahn, "Free-space optical communication through atmospheric turbulence channels," IEEE Transactions on communications **50**, 1293-1300 (2002).

85. L. C. Andrews and R. L. Phillips, *Laser beam propagation through random media* (SPIE press Bellingham, WA, 2005), Vol. 152.

86. J. D. Barchers, D. L. Fried, D. J. Link, G. A. Tyler, W. Moretti, T. J. Brennan, and R. Q. Fugate, "Performance of wavefront sensors in strong scintillation," in *Adaptive Optical System Technologies II*, (International Society for Optics and Photonics, 2003), 217-228.

87. J. K. Wallace, S. Rao, R. M. Jensen-Clem, and G. Serabyn, "Phase-shifting Zernike interferometer wavefront sensor," in *Optical Manufacturing and Testing IX*, (International Society for Optics and Photonics, 2011), 81260F.

88. Y. Zhao, C. Cai, J. Zhang, X. Cao, L. Wang, S. Li, and J. Wang, "Feedback-enabled adaptive underwater twisted light transmission link utilizing the reflection at the air-water interface," Optics express **26**, 16102-16112 (2018).

89. I. Kim, G. Goldfarb, and G. Li, "Electronic wavefront correction for PSK free-space optical communications," Electron. Lett **43**, 1108-1109 (2007).

90. P. Sillard, D. Molin, M. Bigot-Astruc, K. De Jongh, F. Achten, A. M. Velázquez-Benítez, R. Amezcua-Correa, and C. M. Okonkwo, "Low-differential-mode-group-delay 9-LP-mode fiber," Journal of Lightwave Technology **34**, 425-430 (2016).

91. S. Ö. Arık, K.-P. Ho, and J. M. Kahn, "Group Delay Management and Multiinput Multioutput Signal Processing in Mode-Division Multiplexing Systems," Journal of Lightwave Technology **34**, 2867-2880 (2016).

92. S. O. Arik, D. Askarov, and J. M. Kahn, "MIMO DSP Complexity in Mode-Division Multiplexing," in *Optical Fiber Communication Conference*, (Optical Society of America, 2015), Th1D. 1.

93. S. Ö. Arık, K.-P. Ho, and J. M. Kahn, "Delay Spread Reduction in Mode-Division Multiplexing: Mode Coupling Versus Delay Compensation," Journal of Lightwave Technology **33**, 4504-4512 (2015).

94. Y. Wakayama, D. Soma, K. Igarashi, H. Taga, and T. Tsuritani, "Intermediate mode interchange for reduction of differential mode-group delay in weakly-coupled 6-mode fiber

transmission line," in *Optical Fiber Communications Conference and Exhibition (OFC), 2016*, (IEEE, 2016), 1-3.

95. A. Vahdat, H. Liu, X. Zhao, and C. Johnson, "The emerging optical data center," in *Optical Fiber Communication Conference*, (Optical Society of America, 2011), OTuH2.

96. D. M. Kuchta, C. Schow, A. Rylyakov, J. Proesel, F. Doany, C. Baks, B. Hamel-Bissell, C. Kocot, L. Graham, and R. Johnson, "A 56.1 Gb/s NRZ modulated 850nm VCSEL-based optical link," in *Optical Fiber Communication Conference and Exposition and the National Fiber Optic Engineers Conference (OFC/NFOEC), 2013*, (IEEE, 2013), 1-3.

97. D. Molin, M. Bigot-Astruc, G. Kuyt, G. Mélin, and P. Sillard, "Multimode fibers for cost-effective high-speed, short-range networks," in *European Conference and Exhibition on Optical Communication*, (Optical Society of America, 2012), Th. 1. B. 3.

98. J. M. Castro, R. Pimpinella, B. Kose, Y. Huang, B. Lane, K. Szczerba, P. Westbergh, J. Gustavsson, A. Larsson, and P. A. Andrekson, "50 Gb/s 4-PAM over 200 m of high bandwidth MMF using a 850 nm VCSEL," in *Optical Fiber Communication Conference*, (Optical Society of America, 2015), W1D. 1.

99. S. Personick, "Time dispersion in dielectric waveguides," Bell System Technical Journal **50**, 843-859 (1971).

100. J. Fang, A. Li, and W. Shieh, "Low-DMD few-mode fiber with distributed long-period grating," Opt. Lett. **40**, 3937-3940 (2015).

101. H. Liu, H. Wen, B. Huang, Z. Li, and G. Li, "Low-cost and low-loss conversion of OM3 to OM4 MMFs using strong mode mixing," Optics Express **27**, 5581-5587 (2019).

102. J. Abbott, S. Bickham, P. Dainese, and M.-J. Li, "Fibers for short-distance applications," Optical Fiber Telecommunications, 243 (2013).

103. C. Askins, M. Putnam, G. Williams, and E. Friebele, "Stepped-wavelength optical-fiber Bragg grating arrays fabricated in line on a draw tower," Opt. Lett. **19**, 147-149 (1994).

104. I. Giles, A. Obeysekara, R. Chen, D. Giles, F. Poletti, and D. Richardson, "Fiber LPG mode converters and mode selection technique for multimode SDM," IEEE Photon. Technol. Lett. **24**, 1922-1925 (2012).

105. M.-J. Li, "Novel optical fibers for data center applications," in *Broadband Access Communication Technologies X*, (International Society for Optics and Photonics, 2016), 977205.

106. D. Molin, M. Bigot, F. Achten, A. Amezcua, and P. Sillard, "850-950nm wideband OM4 multimode fiber for next-generation WDM systems," in *Optical Fiber Communication Conference*, (Optical Society of America, 2015), M3B. 1.

107. P. Sillard, D. Molin, M. Bigot-Astruc, K. de Jongh, and F. Achten, "Low-Differential-Mode-Group-Delay 9-LP-Mode Fiber," in *Optical Fiber Communication Conference*, (Optical Society of America, 2015), M2C. 2.

108. C. C. C. Carrero, G. Le Cocq, B. Sevigny, A. Lerouge, Y. Quiquempois, M. Bigot, and P. Sillard, "Using advanced S2 analysis to measure mode coupling in a 2-LP-Mode Fiber," in *Optical Fiber Communication Conference*, (Optical Society of America, 2016), W4F. 5.

109. B. Sévigny, G. Le Cocq, G. Bouwmans, Y. Quiquempois, C. C. C. Carrero, and P. Sillard, "Advanced S2 imaging spatial mode analysis: furthering modal characterization," in *SPIE OPTO*, (International Society for Optics and Photonics, 2016), 97740N-97740N-97747.

110. S. Savin, M. Digonnet, G. Kino, and H. Shaw, "Tunable mechanically induced long-period fiber gratings," Opt. Lett. **25**, 710-712 (2000).

111. A. M. Vengsarkar, P. J. Lemaire, J. B. Judkins, V. Bhatia, T. Erdogan, and J. E. Sipe, "Long-period fiber gratings as band-rejection filters," Lightwave Technology, Journal of **14**, 58-65 (1996).

112. K.-P. Ho and J. M. Kahn, "Mode-dependent loss and gain: statistics and effect on mode-division multiplexing," Optics express **19**, 16612-16635 (2011).

113. K.-P. Ho and J. M. Kahn, "Statistics of group delays in multimode fiber with strong mode coupling," Lightwave Technology, Journal of **29**, 3119-3128 (2011).

114. T. Erdogan, "Fiber grating spectra," Lightwave Technology, Journal of **15**, 1277-1294 (1997).

115. Y.-C. Lu, W.-P. Huang, and S.-S. Jian, "Full vector complex coupled mode theory for tilted fiber gratings," Optics express **18**, 713-725 (2010).

116. T. Sakamoto, T. Mori, M. Wada, T. Yamamoto, F. Yamamoto, and K. Nakajima, "Fiber twisting-and bending-induced adiabatic/nonadiabatic super-mode transition in coupled multicore fiber," Journal of Lightwave Technology **34**, 1228-1237 (2016).

117. R. O. Soeiro, T. M. Alves, and A. V. Cartaxo, "Inter-core crosstalk in weakly coupled MCFs with arbitrary core layout and the effect of bending and twisting on the coupling coefficient," Optics Express **27**, 74-91 (2019).

118. S. Yerolatsitis, I. Gris-Sánchez, and T. Birks, "Adiabatically-tapered fiber mode multiplexers," Optics express **22**, 608-617 (2014).